Design, Fabrication, and Analysis of Chemical Hydride-Based Micro Fuel Cells

A Dissertation
SUBMITTED TO THE FACULTY OF
UNIVERSITY OF MINNESOTA
BY

Steven J. Eickhoff

IN PARTIAL FULFILLMENT OF THE REQUIREMENTS
FOR THE DEGREE OF
DOCTOR OF PHILOSOPHY

Tianhong Cui, Adviser

July 2013

To my parents, Al and Mary

Abstract

The performance of portable electronic devices (e.g. cell phones, tablets, laptops) is limited by the energy density of the batteries that power them. Extensive and ongoing research to develop better power sources to replace batteries has largely failed to deliver a viable replacement.

The current research focuses on developing and characterizing a AA form factor micro fuel cell (MFC) which achieves higher energy density than conventional batteries and MFCs. The ultimate goal of this research is to develop a MFC technology that is a viable replacement for primary and secondary batteries in a broad range of consumer portable devices, enabling substantially longer run time, enhanced performance, and the ability to operate independently of the electrical grid.

The AA MFC described herein is a novel integration of a water-recycling hydrogen-air proton exchange membrane (PEM) fuel cell and a chemical hydride-based hydrogen generator. Hydrogen is produced in the hydrogen generator via hydrolysis reaction between a solid chemical hydride and water vapor. Hydrogen and oxygen from air react at the fuel cell, generating electrical energy, water vapor, and waste heat. Water vapor is recovered directly through the fuel cell to generate additional hydrogen, thus the hydrogen generation process can be considered "water-less" in that the water required for the hydrogen generator is derived from the fuel cell and ambient air. The hydrogen generation rate is regulated by a passive (zero power consumption) pneumatic diaphragm valve, which controls diffusive transport of water vapor from the fuel cell to the chemical

hydride based on the pressure difference between the interior of the MFC and the ambient environment.

A two-cell planar PEM fuel cell (series connected, 1.5V nominal output) was developed and evaluated over a range of conditions. Power density of $180 mW cm^{-2}$ was demonstrate with hydrogen fuel, and a total power of $150 mW$ was demonstrated with $LiAlH_4$ fuel, meeting the performance targets for the AA MFC.

Several hydride fuel chemistries were evaluated for reaction rate and practical energy density in a vapor-hydrolysis reactor, and $LiAlH_4$ was selected for use in the AA MFC. Further experiments exploring the impact of hydride particle size and void fraction on reaction rate and yield were conducted, and an improved fuel formulation (5µm particle size, 32% void fraction) was selected.

A pneumatic diaphragm valve was developed and evaluated for open and closed conductance, hysteresis, and repeatability. The valve met its performance targets for each, and achieved a leak rate (proportional to closed conductance) that was >10X smaller than is required for stability.

Fully integrated AA MFCs were evaluated under constant current (20mA) and constant potential (1.2V) discharge tests, using three fuel formulations (crushed pellets, polydisperse powder, monodisperse powder). First generation MFCs using crushed pellets demonstrated $532 Whl^{-1}$ and low reaction yield (60%) resulting from unreacted hydride in the core of the larger fuel particles. First generation MFCs using polydisperse powdered fuel demonstrated higher energy density ($688 Whl^{-1}$) but still had low reaction yield (64%) resulting from unreacted fuel in the core of the larger fuel particles. Second

generation MFCs utilizing an improved fuel formulation (5μm monodisperse particles, 32% void fraction) demonstrated higher average power, reaction yield, and total extracted energy vs. the first generation devices. The highest performing second generation MFC demonstrated a reaction yield of 93% and $1003 Whl^{-1}$, the highest ever reported in a MFC, and equivalent to ~3X greater than conventional AA alkaline batteries.

Table of Contents

List of Tables

List of Figures

Chapter 1: Introduction

The performance of portable electronic devices (e.g. cell phones, tablets, laptops, etc) is limited by the energy density of the batteries that power them. Extensive and ongoing research to develop better power sources to replace batteries has largely failed to deliver a viable replacement.

The current research effort focuses on developing and characterizing a AA form factor micro fuel cell (MFC) which achieves higher energy density than conventional AA batteries and MFCs. The AA MFC is a novel integration of a hydrogen-air proton exchange membrane (PEM) fuel cell and a chemical hydride-based hydrogen generator. The ultimate goal of this research is to develop a MFC technology that is a viable replacement for primary and secondary batteries in a broad range of consumer portable devices, enabling substantially longer run time, enhanced performance, and the ability to operate independently of the electrical grid.

1.1 Background

1.1.1 Micro Power Generation

The design of portable consumer devices reflects a compromise among competing interests ranging from size and performance to run time. While the performance of portable devices as quantified by disk capacity, CPU speed, and available memory continues to advance at a geometric rate approximating Moore's Law (doubling

approximately every 18 months), battery performance as quantified by energy density (energy per unit volume) is advancing linearly (Fig. 1.1), creating an ever-widening gap between the potential and realized performance of portable devices [1.1].

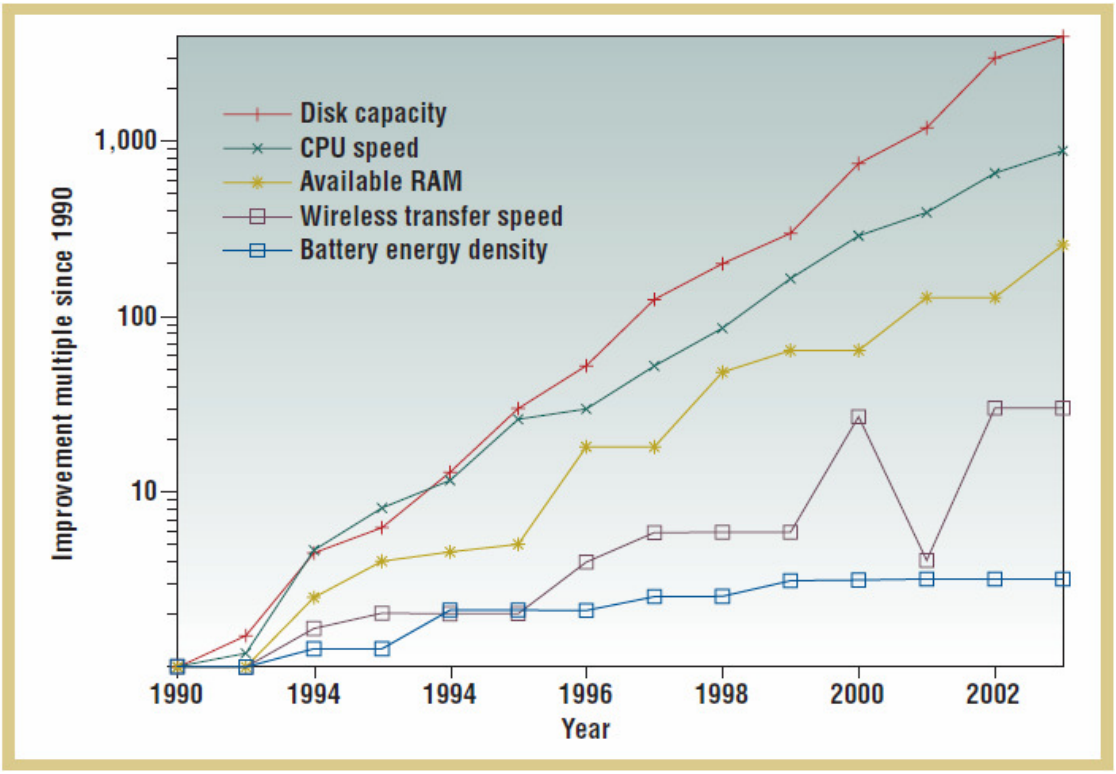

Fig. 1.1: Improvements in the performance of portable electronic device components from 1990 to 2003 [1.1]

This performance gap has spurred research into a range of micro power generation (MPG) technologies ranging from electrochemical devices such as MFCs to micro heat engines (internal combustion, thermoelectric, thermionic, magnetohydrodynamic, etc).

Fuel cells are an attractive approach to MPG for many reasons including their potential for design simplicity, high efficiency, scalability, and broad environmental

range. An overview of the different types of fuel cell technologies is presented in Section 1.1.2, and the range of MFC-based approaches to MPG is outlined in Section 1.1.3.

1.1.2 Fuel Cell Technologies

A fuel cell is an electrochemical energy converter that transforms the chemical energy of a fuel directly into DC electricity. Typically, converting a fuel to electricity requires a thermodynamic cycle comprising several steps, for example, combusting the fuel to generate heat, boiling water with the heat to generate steam, converting the thermal energy of the steam to mechanical energy in a turbine, and finally, converting the mechanical energy of the turbine into electrical energy in a generator. Each of these energy conversion processes imposes a penalty in the form of an efficiency which reduces the amount of useful energy that is available to the next step, the accumulation of which can lead to low overall fuel-to-electrical energy efficiency. A fuel cell circumvents these processes and generates electricity in a single step. It is in-part this promise of simplicity and higher energy conversion efficiency that makes fuel cells attractive for power generation.

Fuel cells can be typically categorized by the type of electrolyte they use. Table 1.1 summarizes the different types of fuel cells categorized by electrolyte, and also includes their typical operating temperature range, catalysts, applications, and fuels.

Table 1.1: Comparison of fuel cell technologies categorized by electrolyte

Fuel Cell Type	AFC	PEMFC	PAFC	MCFC	SOFC
Electrolyte	Liquid potasium hydroxide	Solid polymer	Liquid phosphoric acid	Liquid alkali carbonates	Solid metal oxide
Temperature (ºC)	120-250	0-80	150-220	600-700	600-1000
Catalyst	Ni, Ag, metal oxides, Pt	Pt, Pt-Ru	Pt	None	None
Applications	Space (Apollo, Space Shuttle)	Automotive, stationary, portable	Stationary	Stationary	Stationary, portable
Fuels	Hydrogen	Hydrogen, alcohols, acids	Hydrogen	Hydrogen	Hydrogen, hydrocarbons

Alkaline fuel cells (AFC), phosphoric acid fuel cells (PAFC) and molten carbonate fuel cells (MCFC) are used primarily for macro-scale stationary and vehicle power applications. Their liquid electrolytes and high operating temperatures enable high efficiency, but also present significant challenges for miniaturization. Solid oxide fuel cells (SOFC) and proton exchange membrane fuel cells (PEMFC) use solid electrolytes which are more amenable to miniaturization, thus the majority of MPG research is focused on these two fuel cell technologies.

1.1.3 Micro Fuel Cell Approaches and Limitations

There is a vast literature covering a wide range of approaches to MPG based on PEMFC and SOFC technologies; the majority of these approaches can be lumped into six general categories (Table 1.2) as selected by the International Electrotechnical Commission for Portable Fuel Cells [1.2].

Table 1.2: Comparison of PEMFC and SOFC technologies. Fuel energy density values are based on the lower heating value of the fuels, at typical densities and dilution values.

MFC system type	Reformed hydrocarbon SOFC	Metal hydrid PEM	Chemical hydride PEM	Direct methanol PEM	Reformed methanol PEM	Formic acid PEM
Description	Fuel cell uses hydrogen and CO reformed from hydrocarbons	Fuel cell uses hydrogen released from a metal hydride	Fuel cell uses hydrogen released from hydride hydrolysis	Fuel cell uses methanol directly	Fuel cell uses hydrogen reformed from methanol	Fuel cell uses formic acid directly
Fuel	Butane	Metal hydride	Chemical hydride and water	Methanol	Methanol	Formic acid
Fuel cell technology	SOFC	PEM	PEM	PEM	PEM	PEM
Fuel energy density (Whr/l)	7000-8000	1000-3000	2000-7000	3000-5000	3000-5000	1500-2000
Operating temperature (ºC)	600-1000	0-80	0-80	0-80	250-400	0-80
System energy density (Whr/l)	367	51	86	231	90	<100
Example	Lilliputian Systems Nectar	Horizon MiniPAK	Medis "24-7"	Toshiba Dynario	Ultracell XX25	Tekion Formira

Reformed hydrocarbon SOFCs convert a hydrocarbon fuel (typically an energy dense liquid such as butane) to a hydrogen and carbon monoxide-rich gas using a high-temperature (typically 600-1000 ºC) reactor. This gas mixture is fed to the SOFC and converted to electricity. The SOFC, as its name suggests, uses a solid oxide (ceramic) electrolyte to transport oxygen ions from the cathode to the anode.

The different types of PEMFCs can be distinguished by the fuels they use and whether the fuel is directly oxidized at the fuel cell anode or first reformed into a hydrogen-containing gas. All PEMFCs use a polymer electrolyte membrane (proton exchange membrane) to transport protons from anode to cathode.

In metal hydride PEMFCs, hydrogen is stored in the crystal lattice of intermetallic metal hydrides (such as alloys of $LaNi_5$) and released automatically as it is consumed. In chemical hydride PEMFCs, hydrogen is generated by the controlled (hydrolysis) reaction between a chemical hydride and water. In direct methanol PEMFCs, methanol is directly oxidized to protons at the fuel cell anode. In reformed (indirect) methanol PEMFCs, methanol is converted to a hydrogen-containing gas in a high temperature (typically 250-400 ºC) steam reforming process. In formic acid PEMFCs, formic acid is directly oxidized to protons at the fuel cell anode.

The energy densities of the fuels used by the MFCs (Table 1.2) range from $1000-8000 Whl^{-1}$ and generally compare favorably to primary batteries (~3X to ~20X higher than alkaline AA), however the system energy density of even the highest performing examples described in the literature are far lower. For example, Lilliputian Systems has developed a reformed hydrocarbon SOFC that produces 2.5W of electrical power and has a system energy density of $367 Whl^{-1}$ [1.3], or roughly equivalent to AA alkaline primary batteries [1.4]. Toshiba has developed a direct methanol PEM fuel cell that produces 2W of electrical power and has a system energy density of $231 Whl^{-1}$ [1.5]. The remaining MFCs described in Table 1.2 have energy densities less than $100 Whl^{-1}$. Thus, there are no MFC technologies with sufficient energy density to replace batteries in consumer portable devices.

In order to develop a higher performance MFC, it is critical to understand the drivers of poor performance in current MFC technologies. Table 1.3 shows a qualitative

comparison of MFC technologies and the three primary factors that drive system energy density: fuel energy density, fuel cell efficiency, and balance of plant complexity.

Table 1.3: Comparison of MFC technologies focusing on fuel energy density, fuel cell efficiency, and balance of plant complexity

MFC system type	Reformed hydrocarbon SOFC	Metal hydrid PEM	Chemical hydride PEM	Direct methanol PEM	Reformed methanol PEM	Formic acid PEM
Fuel Energy density	High	Low	Low to High	Med	Med	Low
Fuel cell efficiency	High	High	High	Low	High	Med
Balance of plan complexity	High	Low	Low to Med	Low to Med	High	Low to Med

Intuitively, a MFC technology with high fuel energy density, high fuel cell efficiency, and low balance of plant complexity (size, component count, parasitic power consumption) should be capable of achieving high system energy density; this combination is therefore the goal of this research. Of the technologies in Table 1.3, only reformed hydrocarbon SOFCs and chemical hydride PEMFCs have both high fuel energy density and fuel cell efficiency.

In reformed hydrocarbon SOFCs, the complex and bulky balance of plant limits system energy density. The balance of plant (pumps, valves, heat exchangers, thermal insulation, etc) is necessary to achieve the high temperatures and low thermal losses necessary for efficient operation. Unfavorable scaling of thermal losses (increasing surface area to volume ratio) does not favor the small sizes and thin, planar, form factors required for portable devices. Breakthroughs in SOFC system architecture that simplify

the balance of plant and improve thermal management will be required to improve the performance of this technology and make it viable for use in portable devices.

In chemical hydride PEMFCs, the two factors that limit system energy density are the water reactant for the hydrolysis reaction, and the bulky balance of plant (pumps, valves, reservoirs) associated with delivering it to the chemical hydride and managing the reaction byproducts. Breakthroughs in system architecture that eliminate water as an on-board reactant (i.e. through the use of fuel cell water recovery) and bulky balance of plant (i.e. through the use of compact, passive, regulation schemes) will be required to improve the performance of this technology and make it viable for use in portable devices.

1.2 Current Research

The current research focuses on chemical hydride PEM fuel cell technology, and the scientific and engineering challenges that must be addressed to make it viable for use in portable devices. The AA form factor was chosen as the demonstration vehicle for the technology due to its high performance and ubiquity; AA batteries are available world-wide in a wide range of chemistries, electrical configurations, and in both primary and rechargeable configurations.

The design and operating principle of the AA MFC is summarized here for convenience. A detailed discussion of the component development and system integration is provided in Chapters 2-4.

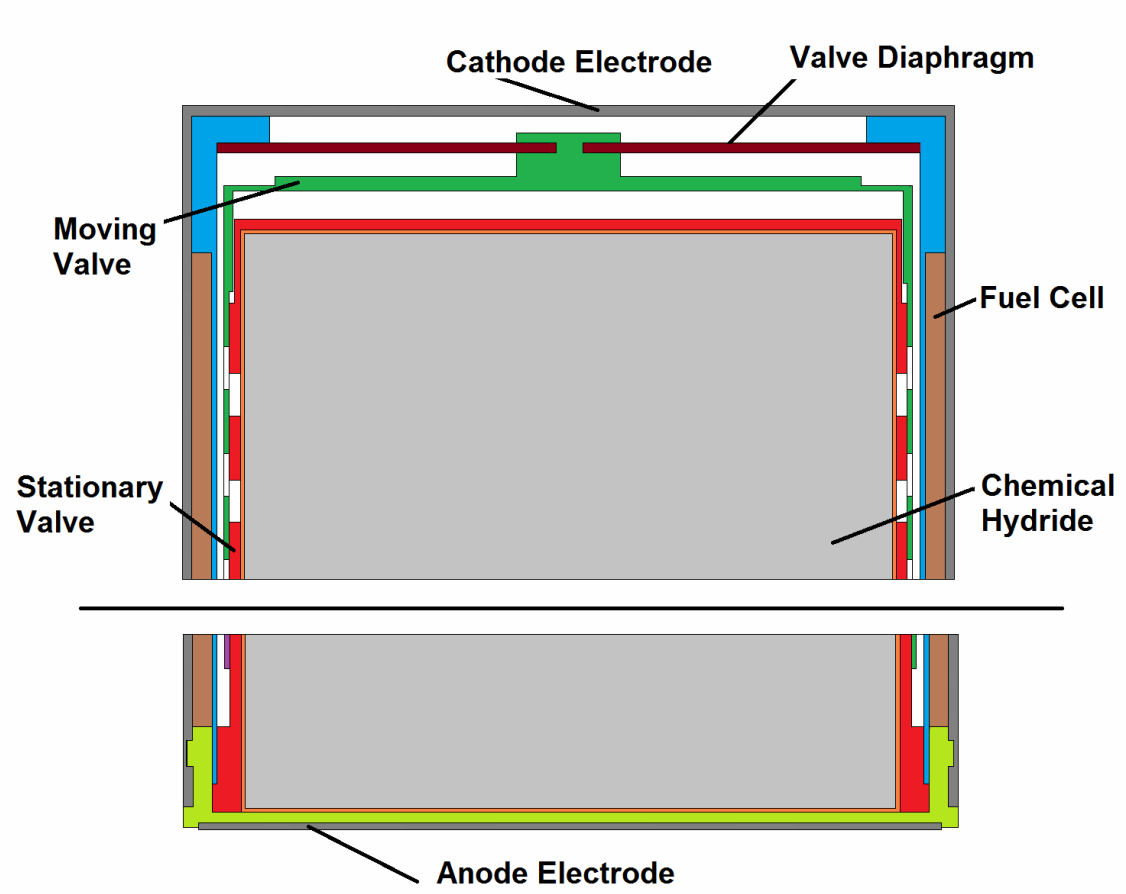

Fig. 1.2: Cross section schematic of the MFC. The middle portion of the MFC is removed to more clearly show the top and bottom.

The AA MFC is comprised of a planar hydrogen-air PEM fuel cell integrated with a self-regulating hydrogen generator. Hydrogen is produced in the hydrogen generator via the hydrolysis reaction between a chemical hydride and water vapor. Hydrogen generated in the hydrogen generator and oxygen from ambient air react at the fuel cell, generating electrical energy, water vapor, and waste heat. Water vapor generated at the fuel cell cathode back-permeates through the PEM and diffuses to the hydride, where it reacts to generate additional hydrogen. The hydrogen generation process can be considered

"water-less" in that it does not require an onboard water reservoir--all of the water required for the hydrogen generator is provided by the fuel cells and ambient air.

The hydrogen generation rate is regulated by a pneumatic diaphragm valve which controls diffusive transport of water vapor from the fuel cells to the chemical hydride, based on the position of the diaphragm. The position of the diaphragm is determined by the pressure difference (ambient minus internal) across it.

When an electrical load is placed on the MFC, hydrogen is consumed by the fuel cell, causing the internal pressure to drop and the diaphragm to deflect inward. This inward deflection opens the valve and allows water vapor to diffuse to and react with the hydride, generating hydrogen. When the load is removed hydrogen consumption stops, causing the internal pressure to rise and the diaphragm to deflect outward. This outward deflection closes the valve and stops water vapor transport to the hydride and hydrogen generation. The valve is partially open under normal operating conditions; it closes or opens completely under no-load or full-load conditions, respectively.

The AA MFC (Fig. 1.3) has a 14mm diameter and 50mm height, and a volume of 7.7cc. It has a nominal operating potential of 0.8 to 1.5 V, and an open circuit potential of ~1.9 V. Power output ranges from 0 to ~150mW, depending on the operating potential, state of discharge, and environmental conditions.

Two circumferentially perforated bands in the metal case provide air to the fuel cells. The cylindrical portion of the metal case functions as the MFC's cathode electrode, while the metal plate at the bottom functions as the anode.

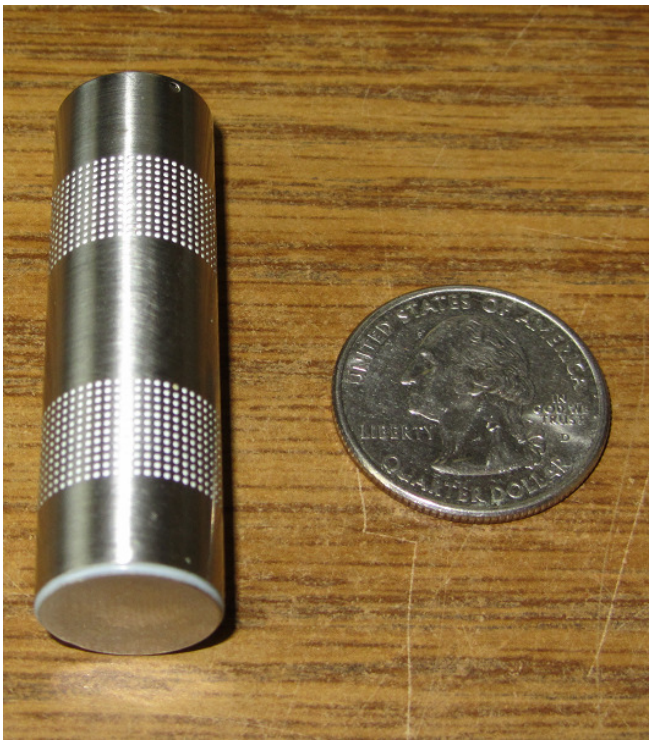

Fig. 1.3: Photograph of the MFC next to quarter for reference.

1.2.1 Research Goals and Objectives

The overall goals and objectives of this research are both fundamental and practical: to understand and overcome the scientific and engineering challenges required to make chemical hydride PEM fuel cells viable for portable power applications, and to demonstrate the technology in a high-volume consumer battery form factor—the AA. Specifically, the following research objectives are addressed as a part of this dissertation:

- To develop a thin, flexible, high power density ($>150 mW cm^{-2}$) planar fuel cell to achieve high energy density at small scales

- To develop a compact, high-conductance, low-leak valve actuated by a pressure-responsive diaphragm, enabling "self-regulated" feedback control with minimal balance of plant
- To develop a chemical hydride vapor hydrolysis-based hydrogen generator which recycles fuel cell-generated water, enabling high fuel conversion efficiency and energy density
- To develop a fully-integrated AA form factor MFC meeting the physical and electrical requirements of conventional AA batteries
- To evaluate, select, and experimentally validate an optimal fuel chemistry for MFCs using vapor-driven hydrolysis
- To develop an improved fuel pellet design (particle size, void fraction) enabling system energy density $>1000 Whl^{-1}$ the highest reported to date for a MFC

1.2.2 Potential Significance of the Research

This research has the potential to enable longer-lasting and higher-performing portable devices with the ability to operate independently of the electrical grid. In the developed world, this may translate to greater physical mobility, connectivity and economic productivity. In the developing world, where wired physical infrastructure is being leapfrogged by wireless portable devices, this research may accelerate existing trends enabled by portable devices, such as mobile internet access, banking, health care, etc.

1.3 Organization of the Dissertation

This dissertation is organized into 5 chapters. Chapter 1 presents the background, state of the art, goals and objectives, and potential significance of this research. Development of the planar PEM fuel cell is presented in Chapter 2, including a discussion of fuel cell chemistry, thermodynamics, kinetics, water balance and recycling, fuel cell design, fabrication, and characterization. Development of the self-regulating hydrogen generator is presented in Chapter 3, including a discussion of the hydride hydrolysis reaction chemistry, hydride evaluation and selection, diaphragm valve, and overall hydrogen generator design, fabrication, and characterization. AA MFC integration, evaluation, and optimization are presented in Chapter 4. Finally, Chapter 5 identifies opportunities for future work.

Chapter 2: Water Recycling Planar PEM Fuel Cell

The core of a PEM fuel cell is the polymer membrane which functions as both a solid electrolyte and a gas separator. The membrane is ionically conductive (conducts protons) but is nominally impermeable to the gaseous reactants (hydrogen and oxygen) and is not electrically conductive (does not conduct electrons). The membrane is coated on both sides with a porous, electrically conductive catalyst electrode which is typically comprised of platinum supported on carbon. The catalyst coated membrane is called a membrane electrode assembly, or MEA. The MEA is sandwiched between porous, electrically conductive gas diffusion layers (GDLs) which are comprised of carbon paper (compressed carbon) or woven carbon cloth. The GDLs allow the gaseous reactants to diffuse to the membrane surface and provide a thermally and electrically conductive path to the current collectors. The MEA and GDL are sandwiched between anode and cathode current collectors, which provide mechanical compression and collect and conduct the current generated by the electrochemical reactions to an external load. A schematic of the planar PEM fuel cell and its operating principle are shown in figure 2.1.

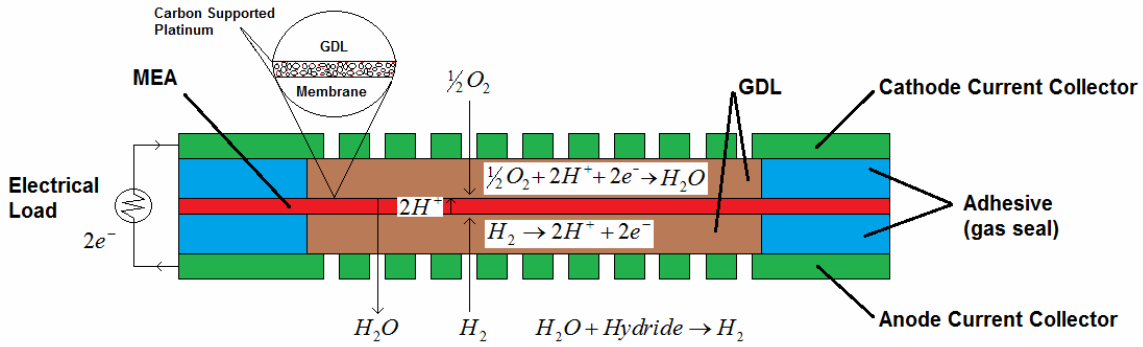

Fig. 2.1: Water-recycling planar PEM fuel cell schematic and principles of operation.

Electrochemical reactions occur at the surface of the catalyst particles which are in contact with the membrane. Hydrogen, which is provided to the anode of the fuel cell, is split into protons and electrons. The protons migrate through the membrane, while the electrons travel through the electrode and current collectors through an electrical load outside of the fuel cell, where they perform work, before returning to the fuel cell cathode. At the cathode, the electrons combine with the protons and oxygen (from ambient air) to form water.

In conventional fuel cells the water generated at the cathode is intentionally lost to the ambient environment to prevent condensation and subsequent air blockage. In water recovery fuel cell (invented by the author and described herein), the water is recovered by back-diffusion directly through membrane and used in a hydrolysis reaction with a chemical hydride to generate hydrogen. Water recovery enables chemical hydride PEM fuel cell designs that don't require water reservoirs--simplifying system design and significantly increasing system-level energy density. Water recovery also impacts fuel cell performance and changes the optimal design of the fuel cell, as described herein.

2.1 Chemistry and Thermodynamics

The electrochemical reactions in PEM fuel cells occur simultaneously at the anode and cathode. Although several other side reactions are possible, the primary reactions are:

Anode reaction: $$H_2 \rightarrow 2H^+ + 2e^- \quad (2.1)$$

Cathode reaction: $$\tfrac{1}{2}O_2 + 2H^+ + 2e^- \rightarrow H_2O \quad (2.2)$$

Overall reaction: $$H_2 + \tfrac{1}{2}O_2 \rightarrow H_2O \quad (2.3)$$

The electrical work done by these reactions is the product of charge and potential:

Electrical work: $$W_{el} = qE \quad (2.4)$$

Where q is the charge and E is the potential. The charge transferred in the fuel cell reactions (equations 2.1-2.3) per mol of hydrogen consumed is:

Charge: $$q = nNq_{el} \quad (2.5)$$

Where n is the number of electrons per molecule of hydrogen, N is Avogadro's number, and q_{el} is the charge of one electron. The product of Avogadro's number and the charge of one electron is Faraday's constant (F). The electrical work is then:

Electrical work: $$W_{el} = nFE \quad (2.6)$$

The maximum amount of (electrical) energy available from the reactions occurring in a fuel cell is the Gibbs free energy change:

Electrical work: $$W_{el} = -\Delta G \quad (2.7)$$

The theoretical cell potential of the fuel cell can be determined by combining equations 2.6 and 2.7 and solving for E:

Theoretical fuel cell potential: $$E = \frac{-\Delta G}{nF} \quad (2.8)$$

The values of all of the variables are known, thus the theoretical fuel cell potential can be calculated; at 25ºC, the value is 1.23V. The effects of temperature and pressure on cell potential can be determined by considering their effects on the Gibbs free energy change for the reactions. Without considering the details, the result is:

Cell potential as a function of T, P: $$E_{T,P} = -\left[\frac{\Delta H}{nF} - \frac{T\Delta S}{nF}\right] + \frac{RT}{nF}\ln\left[\frac{P_{H_2}P_{O_2}{}^{0.5}}{P_{H_2O}}\right] \quad (2.9)$$

Thus, the theoretical potential decreases with increasing temperature and increases with increasing reactant pressure due to the dependence of Gibbs free energy on these parameters.

The efficiency of any energy conversion device is defined as the ratio of useful work output to work (energy) input. The energy input for a fuel cell is the enthalpy change (ΔH) for reaction (2.3), while the useful (electrical) work output is the Gibbs free energy change (ΔG) for the reaction as defined above. The theoretical efficiency of a fuel cell is:

Theoretical fuel cell efficiency: $$\eta = \frac{\Delta G}{\Delta H} \tag{2.10}$$

The values of the variables are known, thus the theoretical fuel cell efficiency can be calculated; at 25ºC, the value is 83%. As with the theoretical fuel cell potential, the theoretical fuel cell efficiency decreases with increasing temperature due to the dependence of the reaction enthalpy and entropy on temperature. In practice however, efficiency and cell potential generally rise with increasing temperature due to mass transfer and kinetic considerations; which will be discussed in the next section.

2.2 Electrochemistry

The electrochemical reactions that occur in a PEM fuel cell take place in the fuel cell electrode, which comprises a thin catalyst (Pt) layer sandwiched between the ionomer membrane and an electrically conductive (carbon) substrate. The electrochemical

reactions occur at the interface between the polymer membrane, catalyst, and gas phase, as illustrated in figure 2.2.

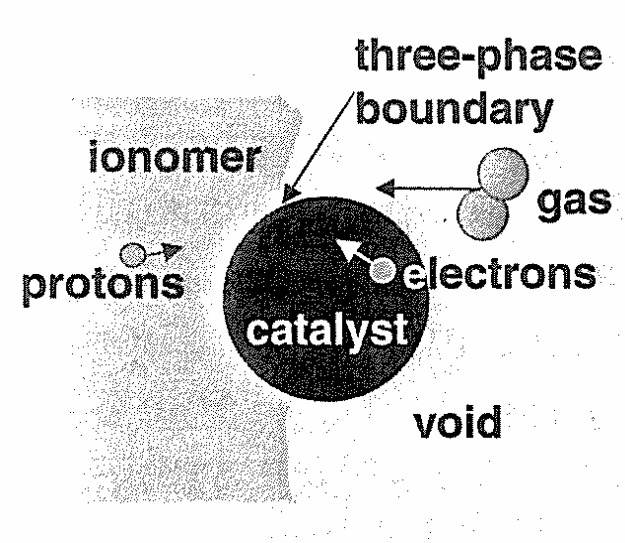

Fig. 2.2: Three phase reaction in the electrode layer of a PEM fuel cell [2.1]

The electrode is a highly-engineered layer whose performance is optimized by balancing the requirements of proton transport in the polymer membrane, electron generation and transport in the catalyst and conductive substrate, and gas phase reactant (hydrogen/oxygen) and byproduct (water vapor) transport in the void space. The kinetics of these reactions are described in section 2.2.1.

2.2.1 Electrode Kinetics

In addition to the Gibbs free energy change that occurs during electrochemical reactions (as described in section 2.1), electrochemical reactions also involve charge transfer. The rate of an electrochemical reaction is determined by an activation energy barrier that the charge must overcome as it is transferred between the ionomer and the

electrode. The current generated by a fuel cell is a measure of the rate at which the electrochemical reactions are occurring. Current density, or current per unit area, is proportional to the charge transferred and to the consumption of reactants per unit area:

Current density: $$i = nFj \tag{2.11}$$

Where n is the number of electrons per mol of reactant, F is Faraday's constant, and j is the reactant flux.

In hydrogen/oxygen fuel cells, hydrogen is stripped of its electrons (oxidized) at the anode electrode, while oxygen gains electrons (is reduced) and water is produced at the cathode. For an electrode in equilibrium (no external current), oxidation and reduction reactions occur at equal rates. These reactions can be described generally as:

Oxidation: $$\mathrm{Re}\,d \rightarrow Ox + ne^{-} \tag{2.12}$$

Reduction: $$Ox + ne^{-} \rightarrow \mathrm{Re}\,d \tag{2.13}$$

Equilibrium: $$Ox + ne^{-} \leftrightarrow \mathrm{Re}\,d \tag{2.14}$$

The consumption of reactants is proportional to their concentration at the surface of the electrode. The reactant consumption rate (flux) corresponding to the forward reaction of the equilibrium reaction (2.14) is:

Forward consumption rate: $$j_f = k_f C_{Ox} \tag{2.15}$$

Where k_f is the forward rate coefficient and C_{Ox} is the surface concentration. A similar expression can be developed for the backward reaction:

Backward consumption rate: $$j_b = k_b C_{Rd} \tag{2.16}$$

Where k_b is the forward rate coefficient and C_{Rd} is the surface concentration. Reactions 2.15 and 2.16 either produce or consume electrons; the net current is the difference between the rates at which electrons are produced and consumed by the forward and backward reactions:

Net current: $$i = nF(k_f C_{Ox} - k_b C_{Rd}) \tag{2.17}$$

In equilibrium the net current is zero, and the reactions proceed in both directions at the same rate. This rate is called the exchange current density.

The reaction rate coefficient for an electrochemical reaction is a function of the Gibbs free energy [2.2]:

Reaction rate coefficient: $$k = \frac{k_b T}{h} \exp\left(\frac{-\Delta G}{RT}\right) \tag{2.18}$$

Where k_B is Boltzmann's constant and h is Planck's constant. The Gibbs free energy for electrochemical reactions is the sum of the chemical and electrical terms:

Gibbs free energy for reduction: $$\Delta G = \Delta G_{Ch} + \alpha_{Rd} FE \quad (2.19)$$

Gibbs free energy for oxidation: $$\Delta G = \Delta G_{Ch} + \alpha_{Ox} FE \quad (2.20)$$

Where the subscript Ch indicates the chemical component of Gibbs free energy, α is the transfer coefficient, F is Faraday's constant, and E is the potential. The transfer coefficient is an experimental parameter which is determined by the slowest step in the reaction (rate determining step). In hydrogen/oxygen fuel cells using platinum catalyst, the value of the transfer coefficient is typically between 0.2 and 2 [2.3]. The forward and backward rate coefficients (2.17) can be expressed as:

Forward rate coefficient: $$k_f = k_{0,f} \exp\left(\frac{-\alpha_{Rd} FE}{RT}\right) \quad (2.21)$$

Backward rate coefficient: $$k_b = k_{0,b} \exp\left(\frac{-\alpha_{Ox} FE}{RT}\right) \quad (2.22)$$

The net current density is obtained by introducing (2.21) and (2.22) into (2.17):

Net current density: $$i = nF\left(k_{0,f} C_{Ox} \exp\left(\frac{-\alpha_{Rd} FE}{RT}\right) - \left(k_{0,b} C_{Rd} \exp\left(\frac{-\alpha_{Ox} FE}{RT}\right)\right)\right) \quad (2.23)$$

At equilibrium, the net current is zero and the potential is E_r, thus the exchange current density for the forward and backward reactions can be expressed as:

Forward exchange current density: $$i_0 = nFk_{0,f}C_{Ox}\exp\left(\frac{-\alpha_{Rd}FE_r}{RT}\right) \quad (2.24)$$

Backward exchange current density: $$i_0 = nFk_{0,b}C_{Rd}\exp\left(\frac{-\alpha_{Ox}FE_r}{RT}\right) \quad (2.25)$$

Combining equations (2.24) through (2.26) leads to an equation relating the current and potential called the Butler-Volmer equation:

Current: $$i = i_0\left[\exp\left(\frac{-\alpha_{Rd}F(E-E_r)}{RT}\right) - \exp\left(\frac{-\alpha_{Ox}F(E-E_r)}{RT}\right)\right] \quad (2.26)$$

Equation (2.26) is valid for both the cathode and anode, however since the overpotential on the anode is positive ($E > E_r$) and the first term is small compared to the second and can be neglected, the current on the anode can be expressed as:

Current on the anode: $$i_a = -i_{0,a}\exp\left(\frac{\alpha_{Ox,a}F(E_a - E_{r,a})}{RT}\right) \quad (2.27)$$

Similarly, the overpotential on the cathode is negative ($E < E_r$), which makes the second term small compared to the first and can be neglected, leading to an expression for the current on the cathode as:

Current on the cathode:
$$i_c = -i_{0,c} \exp\left(\frac{\alpha_{Rd,c} F (E_c - E_{r,c})}{RT}\right) \tag{2.28}$$

Exchange current density (i_0) is a measure of an electrode's propensity to proceed with an electrochemical reaction; the higher the exchange current density, the more current is generated for a given potential. It is analogous to the rate constant for chemical reactions and depends on temperature; however unlike the rate constant, it also depends on concentration. If a reference exchange current density is defined under a certain temperature and pressure, and per unit catalyst surface area, then an expression for the exchange current density at any other temperature and pressure can be defined as [2.4]:

Exchange current density:
$$i_0 = i_0^{ref} a_c L_c \left(\frac{P_r}{P_r^{ref}}\right)^{\gamma} \exp\left[-\frac{E_c}{RT}\left(1 - \frac{T}{T_{ref}}\right)\right] \tag{2.29}$$

Where i_0^{ref} is the reference exchange current density per unit area, a_c is the catalyst specific area, L_c is the catalyst loading, P_r is the reactant partial pressure, P_r^{ref} is the reference pressure, γ is the pressure coefficient (between 0.5 to 1), E_c is the activation energy (66 kJ per mol for oxygen reduction on platinum), R is the gas constant, T is the

temperature, and T_{ref} is the reference temperature. The exchange current density on the anode is several orders of magnitude larger than on the cathode (10^{-4} vs. 10^{-9}) thus the overpotential on the cathode is much larger than the anode, and the anode contribution to overpotential is often neglected, thus the cell voltage-current relationship is often approximated using equation (2.28).

2.2.2 Potential Losses

Potential losses in fuel cells arise from several sources, including slow electrochemical reaction kinetics, internal currents and reactant crossover, electrical and ionic resistance, and mass transfer resistance.

As described in section 2.2.1, a potential difference called activation polarization is required to initiate the electrochemical reactions. Thus, even without an electrical load (zero net current), a fuel cell supplied with reactant gasses will have a potential difference (open circuit potential) that is less than the theoretical potential—typically less than 1V (compared to 1.23V for a cell at standard temperature and pressure). At potentials near the equilibrium potential (high negative overpotentials on the cathode) the first term in the Butler-Volmer equation (2.26) dominates, and the potential-current relationship can be written as:

Cathode activation overpotential: $$\Delta V_{act,c} = E_{r,c} - E_c = \frac{RT}{\alpha_c F} \ln\left(\frac{i}{i_{0,c}}\right) \qquad (2.29)$$

Similarly for the anode, at high positive overpotentials, the second term in the Butler-Volmer equation dominates, and the potential-current relationship can be written as:

Anode activation overpotential: $$\Delta V_{act,a} = E_{r,a} - E_a = \frac{RT}{\alpha_a F} \ln\left(\frac{i}{i_{0,a}}\right) \tag{2.30}$$

If the anode overpotential is neglected (as is often the case), the cell potential considering only activation polarization can be written as:

Cell potential: $$E_{cell} = E_r - \frac{RT}{\alpha F} \ln\left(\frac{i}{i_0}\right) \tag{2.31}$$

Internal currents arise from electron "leaks," while reactant crossover arises from oxygen and hydrogen permeation through the membrane. Although they have different physical mechanisms and different effects on the cell, both can be accounted for mathematically in an equivalent manner—as a current loss. The total current can be written as the sum of the external (useful) current and the current losses due to internal currents and crossover:

Total current: $$i = i_{ext} + i_{loss} \tag{2.32}$$

Substituting this expression for current into equation (2.28) yields and expression for the cell potential which considers activation polarization and current losses due to internal currents and crossover:

Cell Potential:
$$E_{cell} = E_r - \frac{RT}{\alpha F} \ln\left(\frac{i_{ext} + i_{loss}}{i_0}\right) \tag{2.33}$$

Resistive (Ohmic) losses occur due to resistance to the flow of ions in the electrolyte and resistance to the flow of electrons in the electrode. Both are proportional to current, and can be expressed using Ohm's law:

Resistive losses:
$$\Delta V_{ohm} = iR_i \tag{2.34}$$

Where R_i is the sum of the internal resistances, including ionic, electronic, and contact. Electronic resistance is generally small, while ionic and contact resistances are similar in magnitude under normal fuel cell operating conditions. Ionic resistances can however, be large in fuel cells using cathode water recovery due to low levels of membrane hydration--this will be discussed in detail in section 2.3.

Mass transfer resistance in fuel cell electrodes and gas diffusion layers reduce the reactant concentration at the electrode surface, causing potential losses called concentration polarization. The potential difference caused by reduced surface concentration is given by the Nernst equations as:

Concentration polarization: $$\Delta V = \frac{RT}{nF}\ln\left(\frac{C_b}{C_s}\right) \tag{2.35}$$

Where C_b is the bulk reactant concentration, and C_s is the electrode surface reactant concentration. A relationship between the bulk and surface concentrations can be developed using Fick's First Law:

Fick's First Law: $$N = \frac{D(C_b - C_s)A}{\delta} \tag{2.36}$$

Where N is the reactant flux, D is the diffusion coefficient of the reacting species, A is the electrode area, and δ is the diffusion distance. The consumption rate of reacting species can be described as:

Reactant flux: $$N = \frac{I}{nF} \tag{2.37}$$

Combining equations (2.36) and (2.37) gives and expression for the current density as:

Current density: $$i = \frac{nFD(C_b - C_s)}{\delta} \tag{2.38}$$

The reactant concentration at the electrode surface thus depends on the current density, and increased current density leads to reduced surface concentrations. The surface concentration reaches zero once the reactant consumption rate (current) is equal to the diffusion rate—this current is called the limiting current. The limiting current can be expressed as:

Limiting current density: $$i_L = \frac{nFDC_b}{\delta} \tag{2.39}$$

A relationship for the potential loss due to concentration polarization can be obtained by combining equations (2.35), (2.38), and (2.39), and can be expressed as:

Concentration polarization: $$\Delta V_{conc} = \frac{RT}{nF} \ln\left(\frac{i_L}{i_L - i}\right) \tag{2.40}$$

The relative size of each contribution to cell potential losses is shown in figure 2.3. Activation polarization is by far the largest source of potential losses across all currents. Ohmic and concentration polarization are small at low currents, and increase approximately linearly until the limiting current density it approached.

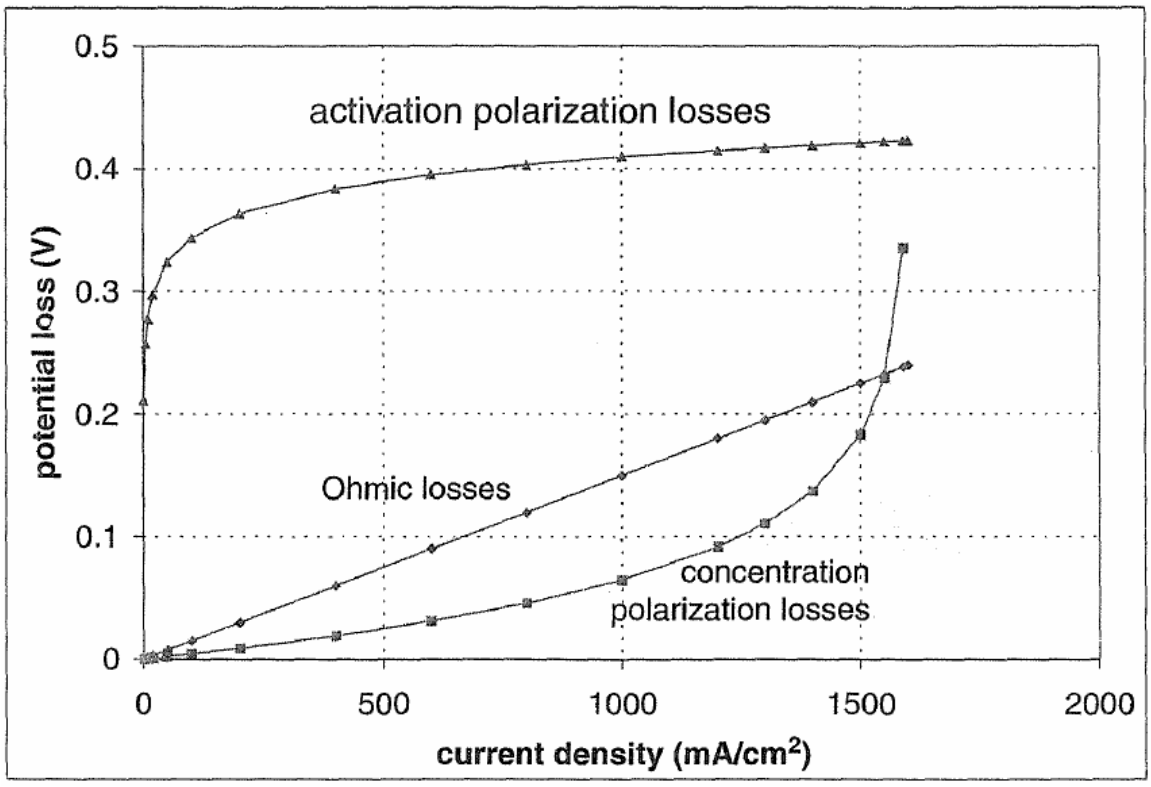

Fig. 2.3: Potential losses in a fuel cell [2.1]

The cell potential combining the activation, Ohmic, and concentration losses can be expressed as:

Cell potential: $$V_{cell} = E_r - (\Delta V_{act} + \Delta V_{conc})_a - (\Delta V_{act} + \Delta V_{conc})_c - \Delta V_{ohm} \qquad (2.41)$$

By introducing equations (2.29) (2.30) (2.34) and (2.40) into equation (2.41), an expression for the cell potential incorporating activation, Ohmic, and concentration can be developed:

Cell potential:

$$E_{cell} = E_{r,T,P} - \frac{RT}{\alpha_c F}\ln\left(\frac{i_{ext}+i_{loss}}{i_{0,c}}\right) - \frac{RT}{\alpha_a F}\ln\left(\frac{i_{ext}+i_{loss}}{i_{0,a}}\right) - \frac{RT}{nF}\ln\left(\frac{i_{L,c}}{i_{L,c}-i_{ext}-i_{loss}}\right) - \frac{RT}{nF}\ln\left(\frac{i_{L,a}}{i_{L,a}-i_{ext}-i_{loss}}\right) - R_{i,i}(i_{ext}+i_{loss}) - i_{ext}(R_{i,e}+R_{i,c}) \quad (2.42)$$

For most applications, a sufficiently accurate expression of the cell potential may be obtained by assuming that the anode losses are small compared to those at the cathode:

Cell potential: $$E_{cell} = E_{r,T,P} - \frac{RT}{\alpha_c F}\ln\left(\frac{i}{i_0}\right) - \frac{RT}{nF}\ln\left(\frac{i_L}{i_L - i}\right) - iR_i \quad (2.43)$$

A fuel cell polarization curve illustrating potential losses (polarization) due to activation, Ohmic, and concentration effects is shown in Fig. 2.4.

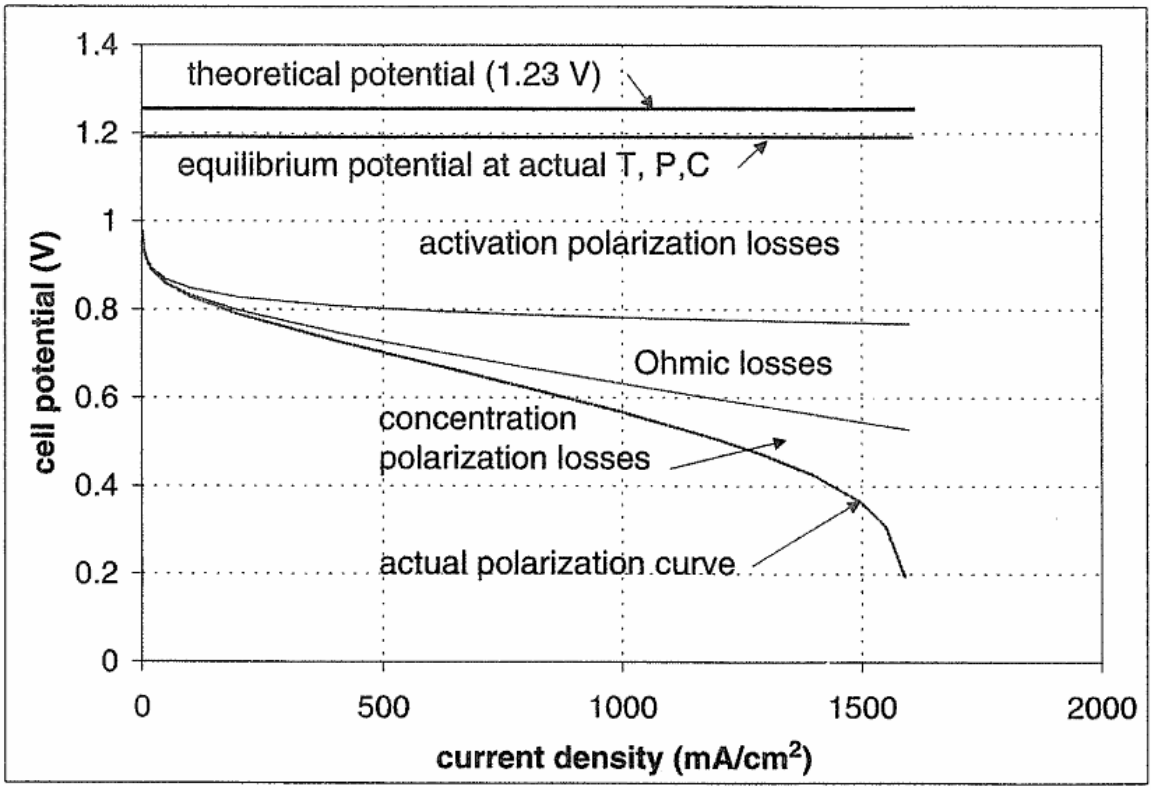

Fig 2.4: Potential losses in a fuel cell, and polarization curve [2.1]

The actual fuel cell polarization curve under typical operating conditions has an open circuit potential of around 1V, a linearly decreasing potential with current from 0.8V to 0.5V, after which the potential drops quickly to zero as the limiting current is approached. The slope of the Ohmic region and the limiting current density are strongly affected by water recovery, as described in the section 2.3.

2.3 Water Transport and Recycling

Water plays several important roles in water recycling PEM fuel cells; it serves as a reaction product of the electrochemical reaction, a fuel for the hydrogen-generating hydrolysis reaction, and its concentration within the membrane strongly impacts fuel cell performance.

PEM fuel cells use solid electrolyte membranes typically constructed from perfluorocarabon-sulfonic acid ionomer (PSA). These membranes must possess a range of properties, including chemical and mechanical stability, low gas permeability, and most importantly, high proton conductivity. PSA membranes derive their proton conductivity from the SO_3H groups (SO_3^- bonded with H^+) which are ionically bonded to the end of the side chains. Figure 2.5 shows the chemical structure of one of the best known ionomers—Nafion.

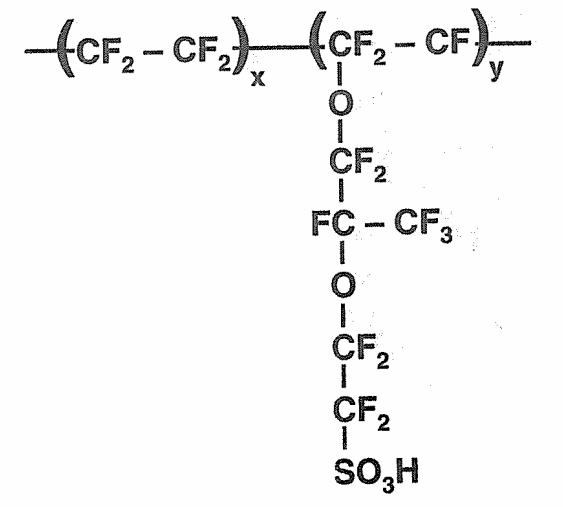

Fig 2.5: Chemical structure of Nafion [2.1]

Due to their ionic nature, the side chains cluster together within the structure of the membrane. The side chains are highly hydrophilic and absorb water, creating channels within the membrane in which protons can easily migrate, making the membrane conductive. The protonic conductivity of the membrane is thus highly dependent on this membrane structure and its water content.

Water content (λ) is typically expressed as the number of water molecules ($N(H_2O)$) per sulfonic acid group ($N(SO_3^-)$) present within the polymer:

Water content: $$\lambda = N(H_2O) / N(SO_3^-) \tag{2.44}$$

The water content of PSA membranes like Nafion, when equilibrated with water vapor, can range from 0.043 when the water activity is zero up to 14 when the water activity is 1. Water activity is equivalent to the relative humidity, which is the ratio of the water vapor pressure to its saturation vapor pressure at a given temperature:

Water activity: $$a = p / p_{sat} \tag{2.45}$$

Zawodzinski *et al.* [2.5] fit a polynomial equation to experimental results, to obtain a relationship between the water activity on the faces of a Nafion membrane and its water content:

Water content: $$\lambda = 0.043 + 17.18a - 39.85a^2 + 36a^3 \tag{2.46}$$

The water concentration in PSA membranes is the product of the sulfonic acid concentration c_f and the water content:

Water concentration: $$c = c_f \lambda \tag{2.47}$$

The conductivity of PSA membranes is a strong function of water content and temperature. Springer *et al.* [2.6] correlated ionic conductivity data and developed a relationship between ionic conductivity and water content and temperature:

Nafion conductivity: $$\kappa = (0.005139\lambda - 0.00326)\exp\left[1268\left(\frac{1}{303} - \frac{1}{T}\right)\right] \tag{2.48}$$

2.3.1 Water Transport

There are several mechanisms for water transport in PSA membranes: water is dragged from anode to cathode by protons due to electroosmotic drag, water is produced at the cathode as a result of the electrochemical reaction (equation 2.2), and water diffuses due to concentration gradients within the membrane.

Water transport (flux) due to electroosmotic drag can be expressed as:

Electroosmotic drag: $$N_{H_2O,drag} = \xi \frac{i}{F} \tag{2.49}$$

Where ξ is the electroosmotic drag coefficient, defined as the number of water molecules per proton. The value of drag coefficient is strongly affected by the water content of the membrane. For low values of water content ($0 \leq \lambda \leq 5$) which are typical in water recycling fuel cells, Fuller and Newman [2.7] found that the drag coefficient decreased rapidly from ~1.4 at $\lambda = 5$ to 0 at $\lambda = 0$ as described by:

Drag coefficient: $$\xi = -BCa\exp(-Ca) \tag{2.50}$$

Where B is -3.4377, C is 1.717, and a is the water activity. The water generated by the electrochemical reaction (flux) is a function of current, and can be expressed as:

Water generation: $$N_{H_2O,gen} = \frac{i}{2F} \tag{2.51}$$

Water generation and electroosmotic drag both contribute to water build-up at the cathode, creating a concentration gradient within the membrane which drives water back from cathode to anode due to diffusion. This back-diffusion rate (flux) can be expressed as:

Water diffusion: $$N_{H_2O,diff} = D\frac{dc}{dz_{memb}} \tag{2.52}$$

Where D is the water diffusion coefficient, dc / dz_{memb} is the concentration gradient in the membrane. The water diffusion coefficient is a function of water content. Motupally *et al.* [2.8] found that the diffusion coefficient can be expressed as:

Diffusion coefficient: $D = 3.1E^{-3}\lambda(e^{0.28\lambda} - 1)\exp\left(\frac{-2436}{T}\right)$ for $0 \leq \lambda \leq 3$ (2.53)

$$D = 4.17E^{-4}\lambda(161e^{-\lambda})1)\exp\left(\frac{-2436}{T}\right) \text{ for } 3 \leq \lambda \leq 17 \quad (2.54)$$

The net transport of water from anode to cathode via back-diffusion is required for water recycling, as described in section 2.3.2.

2.3.2 Water Recycling

Water recycling fuel cells rely on the net transport of water from cathode to anode to generate hydrogen for the fuel cell. Figure 2.6 illustrates water transport in water-recycling PEM fuel cells.

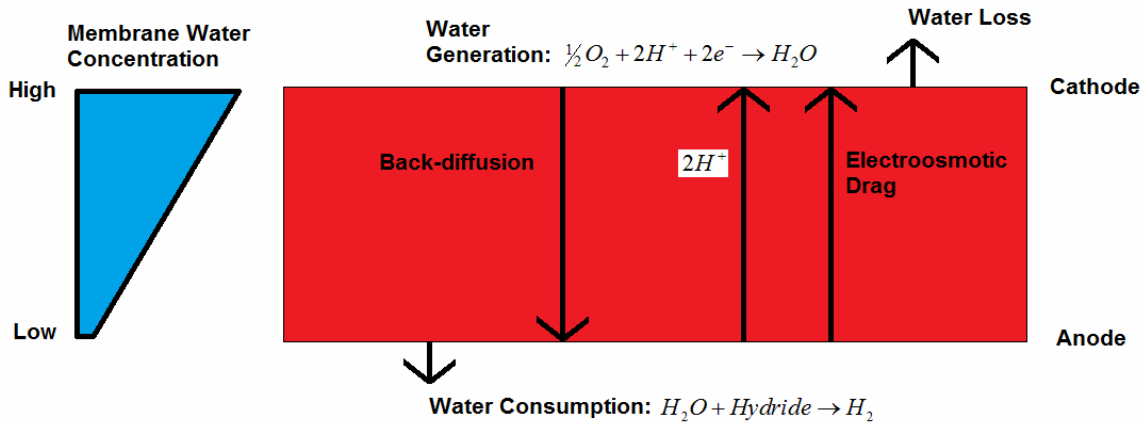

Fig 2.6: Illustration of water transport mechanisms in the membrane of a water-recycling PEM fuel cell

A water balance on the cathode of the PEM can be expressed as:

Water balance: $$N_{H_2O,acc} = N_{H_2O,gen} - N_{H_2O,loss} + N_{H_2O,drag} - N_{H_2O,dif} \quad (2.55)$$

Where $N_{H_2O,acc}$ is the water accumulated at the cathode, $N_{H_2O,gen}$ is the water generated at the cathode due to the electrochemical reaction, $N_{H_2O,loss}$ is the water loss from the cathode to the ambient, $N_{H_2O,drag}$ is the water transport to the cathode due to electroosmotic drag, and $N_{H_2O,dif}$ is the water transport from cathode to anode due to diffusion. Water loss (flux) to ambient can be expressed as:

Water loss: $$N_{H_2O,loss} = D\frac{dc}{dz_{amb}} \quad (2.56)$$

Where dc / dz_{amb} is the water concentration gradient from the cathode to the ambient environment. Under steady state conditions, water accumulation at the cathode and losses to ambient must be zero, thus the steady state water balance can be expressed as:

Steady state water balance:
$$\frac{i}{2F} + \xi \frac{i}{F} - D \frac{dC}{dz_{memb}} = 0 \qquad (2.57)$$

Steady state water balance requires that the water concentration at the membrane surface be equal to the ambient concentration, thus the steady state current density of water-recycling fuel cells is dependent on ambient water concentration:

Steady state current density:
$$i = \left(\frac{2FD}{1 + 2\xi} \right) \frac{dc_{amb}}{dz_{memb}} \qquad (2.58)$$

Calculated values for the steady state current density (limited by water transport) as a function of cathode activity, for various values of anode activity at 25ºC, are shown in Fig 2.7. Current density is extremely sensitive to anode activity, which is expected due to the strong dependence of the diffusion coefficient and water content on this parameter. Experimental values for the current density in water recycling fuel cells range from $0.01 - 0.1 Acm^{-2}$ for cathode activity values ranging from 0.1 to 0.9, suggesting that the anode activity is in the range of 0.001 to 0.01.

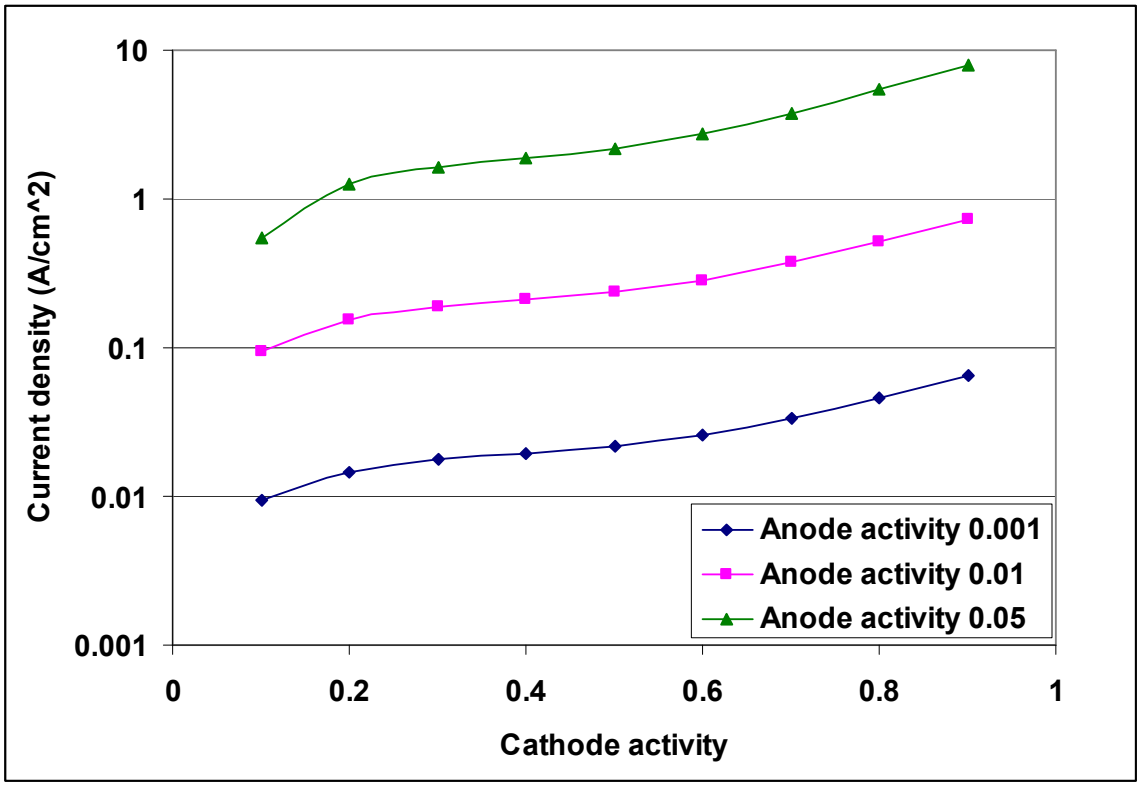

Fig 2.7: Projected steady state current density (limited by water transport) as a function of cathode activity for various values of anode activity at 25ºC

2.4 Fuel Cell Design Considerations

The analysis presented in the previous section leads to a number of important conclusions regarding the design and optimization of water-recycling planar PEM fuel cells. Further, their implementation in the AA battery form factor--and the performance requirements that come with it, place additional requirements on the fuel cell design. The most important design considerations are as follows:

- **Locating the fuel cell on the AA perimeter:** Current density in water recycling planar fuel cells is low (typically $0.01-0.1 Acm^{-2}$) compared to conventional planar fuel cells (typically $>1 Acm^{-2}$), thus meeting the power target (>150mW) will require a large surface area fuel cell (5 to $10\,cm^2$). The only surface of the AA form factor with sufficient area for the fuel cell is the perimeter. Other considerations for placing the fuel cell around the perimeter, relating to diffusion resistance within the fuel, will be discussed in Chapter 3.
- **Minimizing the thickness of the fuel cell:** The fuel cell should be made thin to minimize its volume, (maximize system energy density) enable the flexibility required to wrap around the curved AA form factor perimeter, and to minimize diffusion resistance (maximize power).
- **Two series-connected cells:** AA form factor batteries have operating potentials ranging from 1.6V to 0.8V. Covering this range with a fuel cell requires two series-connect cells, each operating between 0.8V and 0.4V.

2.4.1 Fuel Cell Design

The planar PEM fuel cell (Fig. 2.8) is comprised of 5 layers stacked and compressed together, forming a monolithic and flexible planar fuel cell. The layers consist of an anode electrode, anode adhesive layer with embedded anode gas diffusion layers (GDL), membrane electrode assembly (MEA), cathode adhesive layer with embedded cathode GDL, and cathode electrode.

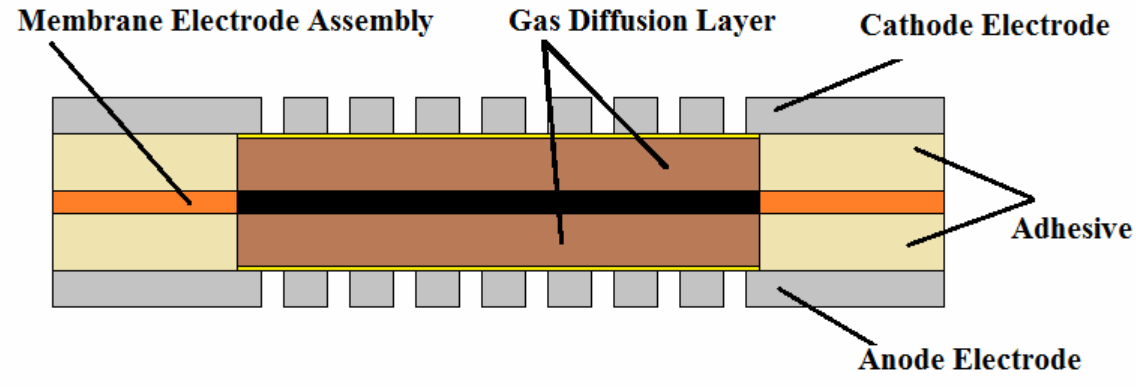

Fig. 2.8: Cross section schematic of the planar fuel cell.

A range of design parameters were considered for each of the planar fuel cell components (electrodes, adhesive, GDL, MEA). These design parameters, the range tested, selected value, and rational are summarized in Table 2.1. The selected values are driven by the design requirements described above, and were determined based on modeling and experimental results which are described in section 2.6.

Table 2.1: Parameters for planar fuel cell design

	Design Parameter	Range tested	Selected value	Rational
Electrode	Substrate material	Polyimide and PET	PET	Good compromise between hydrogen permeability, cost, charing with laser, and metal electrode adhesion
	Substrate thickness (μm)	12 to 100	25	Good compromise between tear resistance and flexibility
	Air hole diameter (mm)	0.5 to 1	1	Good compromise between reactant concentration uniformity, number of holes, and pitch
	Air hole pitch (mm)	0.5 to 2	1.5	Good compromise between reactant concentration uniformity, number of holes, and pitch
	Metal thickess (um)	0.5 to 3	1	Good compromise between cost and electrical resistance
	Active area per cell (cm^2)	3 to 6	4.6	Achieves desired power output
Adhesive	Seal length (mm)	1 to 10	4	Good compromise between adheasive area and leak rates
	Thickness (μm)	38 to 200	100	Defines thickness/compression of gas diffusion layer, factors into reactant concentration uniformity
	Adhesive compound	Acrylic	Acrylic	Good compromise between thickness, flexibility, and adhesion
	Window area	3 to 6	4.6	Defined by active electrode area
GDL	Thickness (μm)	100 to 400	175	Good compromise between compression, contact resistance, and reactant concentration uniformity
	Permeability (Gurley)	15 to 50	50	Good compromise between electrical resistance and reactant concentration uniformity
	Area (cm^2)	3 to 6	4.6	Defined by active electrode area
	Surface coating	Hydrophobic and hydrophillic	Hydrophobic	Improves cathode water recovery, prevents cathode flooding
MEA	Thickness (μm)	15 to 50	15	Achieves highest power density through reduced ionic and water transport resistance
	Formulation	Nafion, Gore Primea	Gore Primea	Better low temperature and low humidity performance
	Catalyst	Gore Primea	Gore Primea	Optimized for low temperature, low humidity performance, air cathode, non-pressurized reactants
	Area (cm^2)	3 to 6	4.6	Achieves desired power output

The fuel cell electrodes (Fig 2.9) are comprised of patterned metal on a thin polymer substrate. Each electrode has a distinct metallization pattern to enable a series electrical connection when the component layers are assembled. The bottom tab on the anode electrode (left) is connected to the anode plate, and forms the negative output electrode for the AA fuel cell. The top tab on the anode electrode (left) is connected to the bottom of the cathode electrode (right) via the L-shaped tab that extends up the left side, connecting the two cells in series. The solid (non-perforated) portion of the top electrode on the cathode (left) connects to the can, which is the cathode output electrode for the AA fuel cell. The PET substrate provides electrical isolation, and due to its low gas permeability, prevents the anode and cathode reactants from mixing.

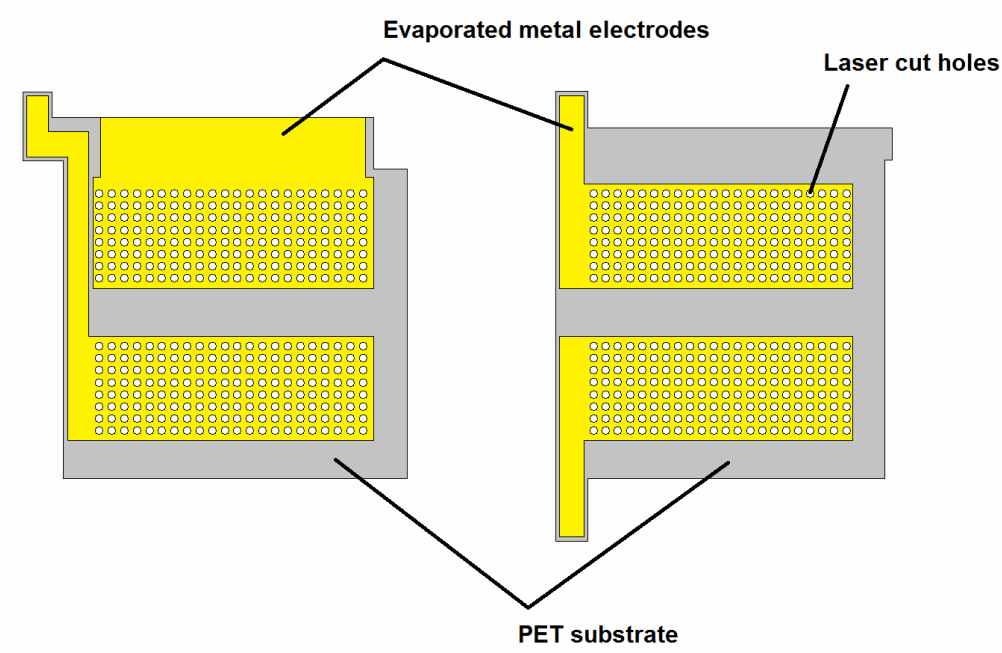

Fig. 2.9: CAD drawings of the fuel cell cathode (left) and anode (right) electrodes

The adhesive layers (Fig 2.10) are comprised of double sided adhesive on a polymer substrate. The adhesive layers mechanically adhere (and seal) the electrode to the polymer frame of the MEA, and define pockets for the (GDLs) which electrically connect the MEA to the metallization pattern on the electrodes.

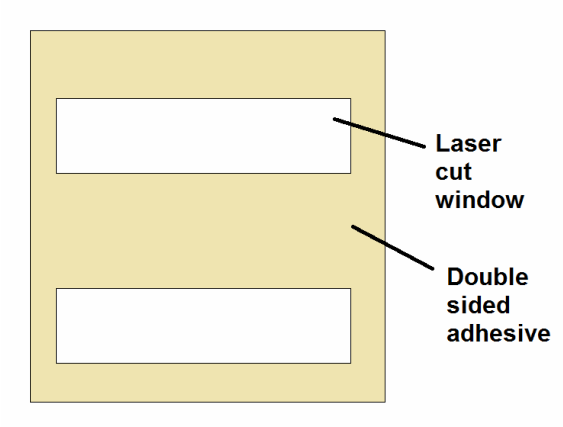

Fig. 2.10: CAD drawing of the anode/cathode adhesive. GDLs are sized to fit inside the two laser-cut windows in the adhesive layer

The MEA in polyimide frame (Fig 2.11) is comprised of two electrically isolated MEA windows (active areas) embedded in a polyimide frame. As described above, the MEA windows (active areas) are connected to the patterned metal portion of the electrodes by the GDLs, while the polyimide frame is adhered to the electrode and forms a gas seal. The MEA windows are the electrochemically active portion of the planar fuel cell, and are responsible for converting the gaseous hydrogen and oxygen reactants to electricity and water vapor, as described above.

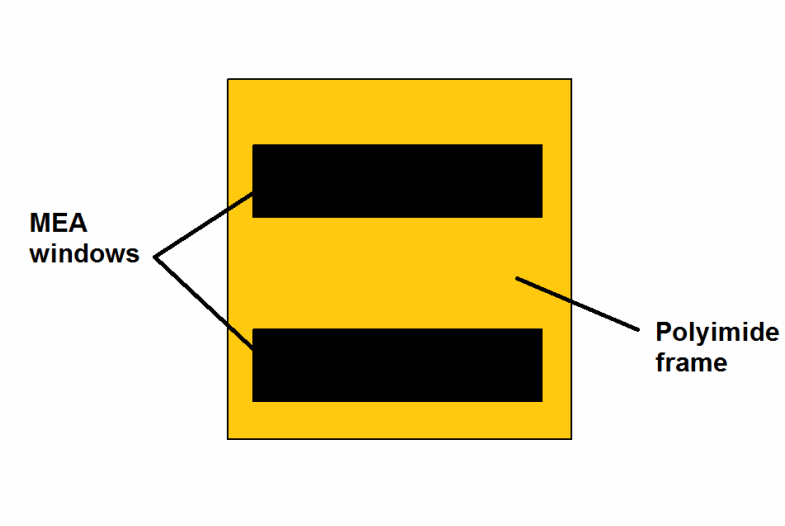

Fig. 2.11: CAD drawing of the MEA in its polyimide frame

2.5 Fuel Cell Fabrication

The anode and cathode electrodes are formed by patterning with shadow masks (Fig 2.12) an evaporated metal film (50 Angstrom Ti, 1 µm Au) on a 25 µm thick PET substrate (Fralock, Valencia, CA). Four cathode or anode electrodes fit within each six-inch diameter ring. The circular holes in the shadow masks deposit test spots which are used to verify metal thickness and metal adhesion strength to the PET substrate.

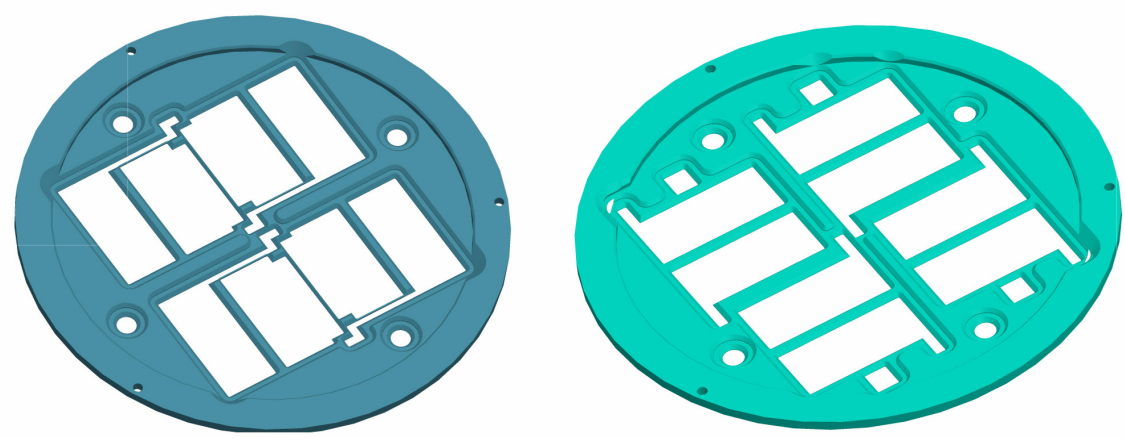

Fig 2.12: Anode (left) and cathode (right) shadow masks for electrode metallization

The electrode perimeter and holes are cut with a laser (Universal Laser Systems, Scottsdale, AZ).

The anode and cathode adhesive layers are three layer stacks comprises a 50 µm thick polyimide layer sandwiched between 25 µm adhesive layers (Fralock, Valencia, CA). The adhesive layers also include release layers which are present to simplify handling and processing, but are removed prior to use in the fuel cell.

The cathode and anode gas diffusion layers comprise 200 µm thick carbon paper (Ballard, Burnaby, BC) cut to fit the "windows" in the adhesive layers.

The MEA in polyimide frame comprises a catalyst electrode coated 25 µm thick Nafion membrane embedded in a 25 µm thick polyimide frame (Ion Power, New Castle, DE). Fig 2.13 shows the planar fuel cell components, arranged (from left to right) in the order in which they are assembled.

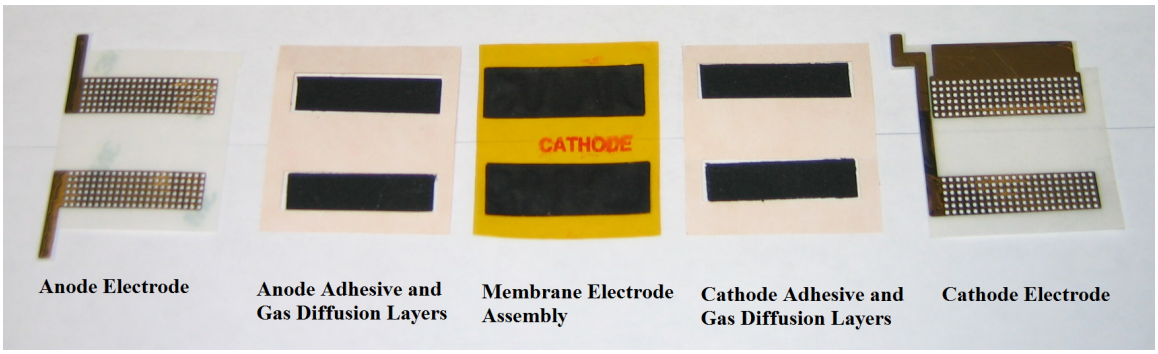

Fig 2.13: Planar fuel cell components arranged (from left to right) in the order in which they are assembled

The planar fuel cell is assembled by sequentially stacking the layers (from left to right) and compressing them together with one metric ton of force using a hydraulic press (Carver, Wabash, IN). The planar fuel cell is then wrapped around and adhered to the anode support. Figure 2.14 shows the assembled planar fuel before (left) and after (right) it has been wrapped around the anode support.

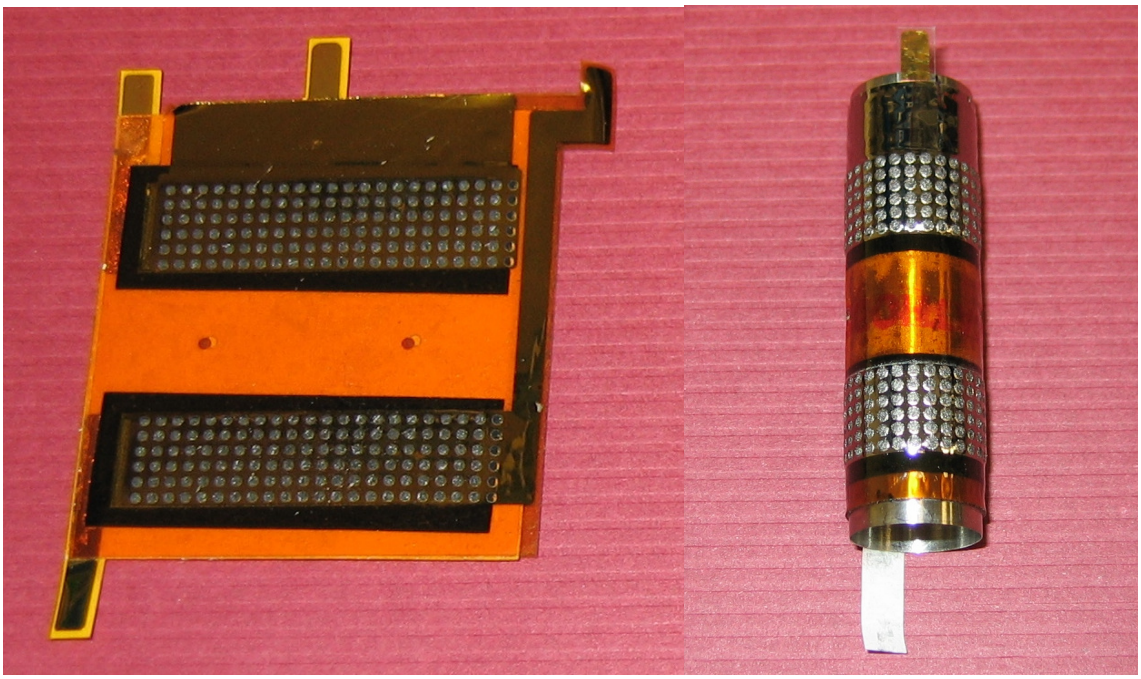

Fig 2.14: Planar fuel cell (left) wrapped around anode support (right)

2.6 Fuel Cell Characterization

The electrical performance of the planar fuel cell is tested with a potentiostat (Maccor, Tulsa, OK). Current and potential are recorded as the cell potential is stepped in 0.1 V increments from the open circuit potential (~1.9V) to 0.8 V. Bottled hydrogen gas (99.999% pure, Toll Gas, Plymouth, MN) at 1 atmosphere pressure flowing at 100 sccm is fed to the interior of the MFC; excess flow is exhausted to ambient. Tests are performed in a temperature and humidity controlled environment at 20 ºC, 50 % relative humidity, using a temperature chamber (Thermotron, Holland MI) and a custom fabricated bubbler system. A PC running Labview is used to control the flow and humidification systems and record the sensor data. A schematic of the fuel cell test bed is shown in figure 2.15.

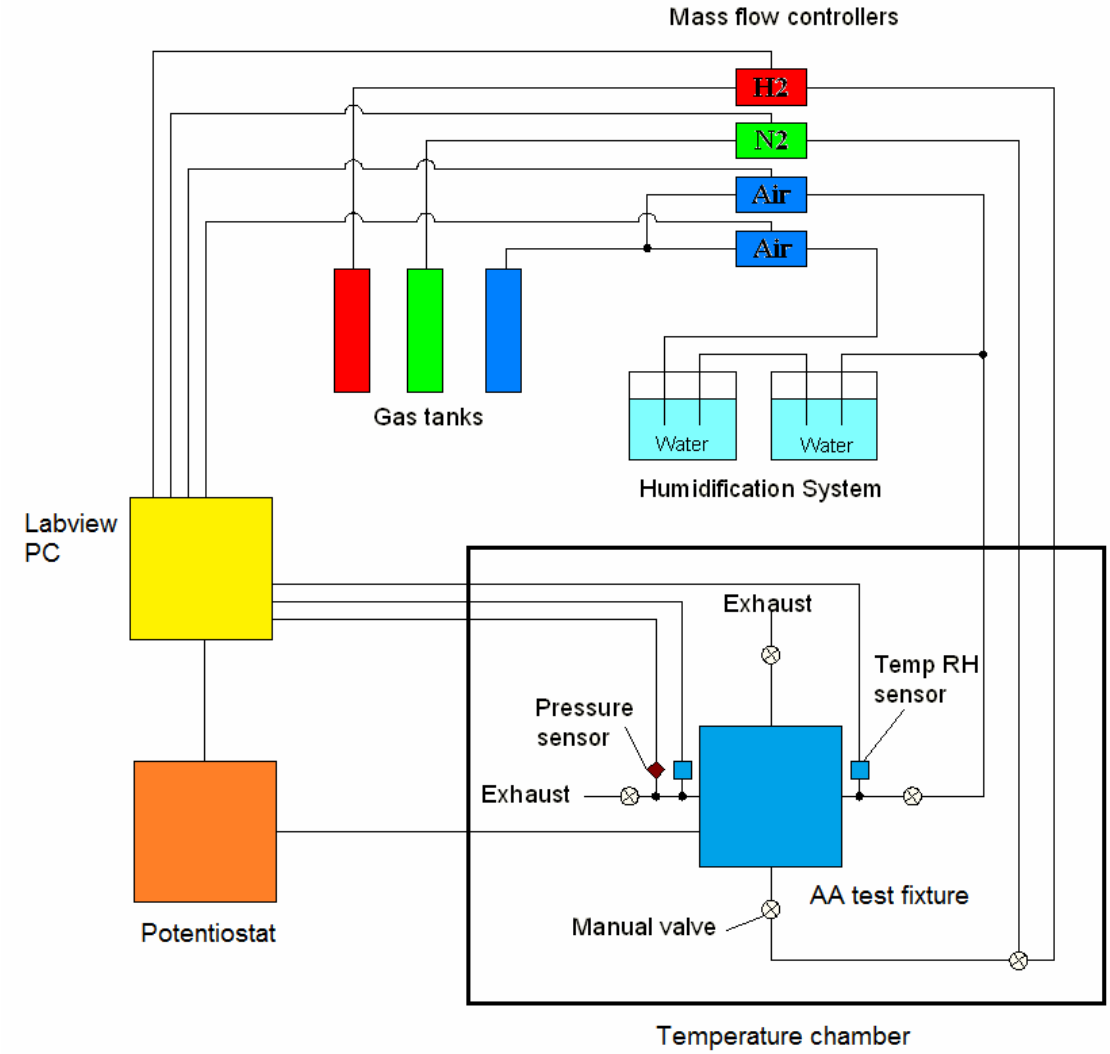

Fig 2.15: Schematic of the fuel cell test bed

2.6.1 Performance Optimization

Compression of the fuel cell (contact resistance) and reactant concentration and uniformity at the MEA surface play a critical role in determining the performance of planar passive fuel cells. In the present planar fuel cell design, the thickness of the adhesive layer is fixed and defines the depth of the pocket in which the GDL is placed. Thus, the thickness and porosity of the GDL can be varied to control the contact

resistance (GDL/MEA, GDL/current collector) and reactant concentration/uniformity at the MEA surface. Fig 2.16 shows the impact on power density of varying the GDL thickness.

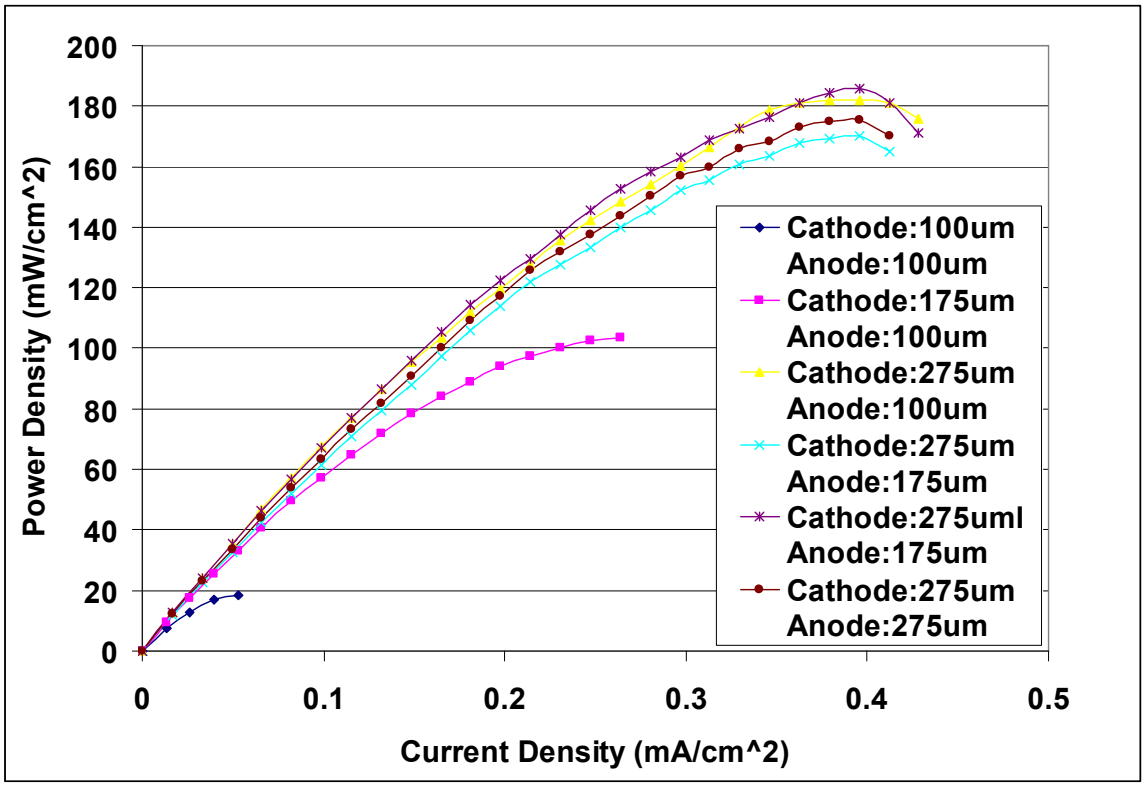

Fig. 2.16: Power curves for different values of cathode and anode GDL thickness

The total GDL thickness (anode plus cathode) was varied between 200 and 550 μm by switching between 100, 175, and 275 μm GLD thicknesses on both the anode and cathode. Peak power density ranged from 20 to 185 $mWcm^{-2}$ over the tested range of GDL thickness, and increased with higher GDL thickness until a maximum was achieved between 375 μm and 450 μm. Further increases in GDL thickness (up to 550 μm) resulted in lower peak power density, likely due to increased diffusion resistance that

negatively impacted reactant concentration/uniformity at the MEA surface. These results were used to select the GDL thickness and active fuel cell area, to achieve the targeted power output in the AA MFC.

2.6.2 AA Fuel Cell Performance

A polarization curve for the selected fuel cell design following integration with the other AA system components (described in Chapeter 4), and running on bottled hydrogen gas is shown in Fig. 2.17. The open circuit potential is 1.9 V, with a peak power of 575 mW occurring at 0.8 V. The AA fuel cell exhibits the typical decrease in potential with increasing current due to activation, Ohmic, and concentration polarization.

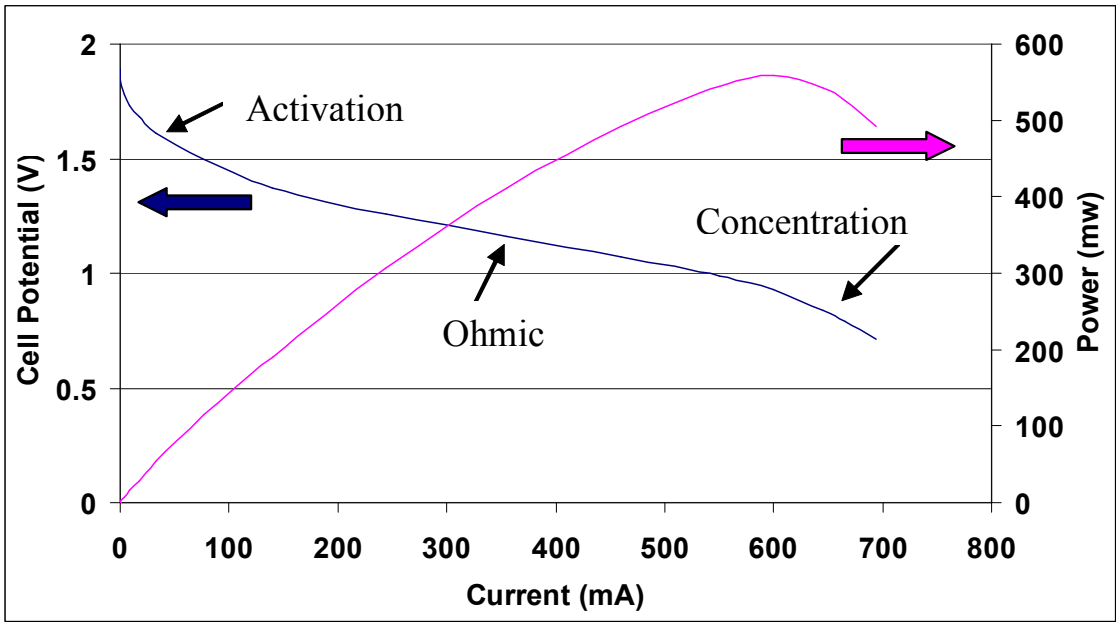

Fig. 2.17: Polarization curve with bottled hydrogen gas. The MFC exhibits the typical decrease in potential with increasing current due to activation, Ohmic, concentration polarization

Similarly, a polarization curve for the AA MFC running on LAH fuel is shown in Fig. 2.18. The open circuit voltage (1.9 V) is similar to the test performed with bottled hydrogen gas, however the peak power is lower (160 mW), and slope of the voltage vs. current curve is larger, indicating higher internal resistance. This is expected for two reasons, as described above: First, the highly hygroscopic LAH is positioned closely to the fuel cell anode to enable fuel cell water recovery. This dries the PEM somewhat and reduces its ionic conductivity (which is strongly depended on hydration), resulting in higher internal resistance. Second, electroosmotic drag (in which water molecules are dragged from anode to cathode by migrating protons) places an upper limit on current density, because the water back-permeation rate in the PEM and consumption rate by the LAH fuel must be balanced to sustain power output in water recycling fuel cells.

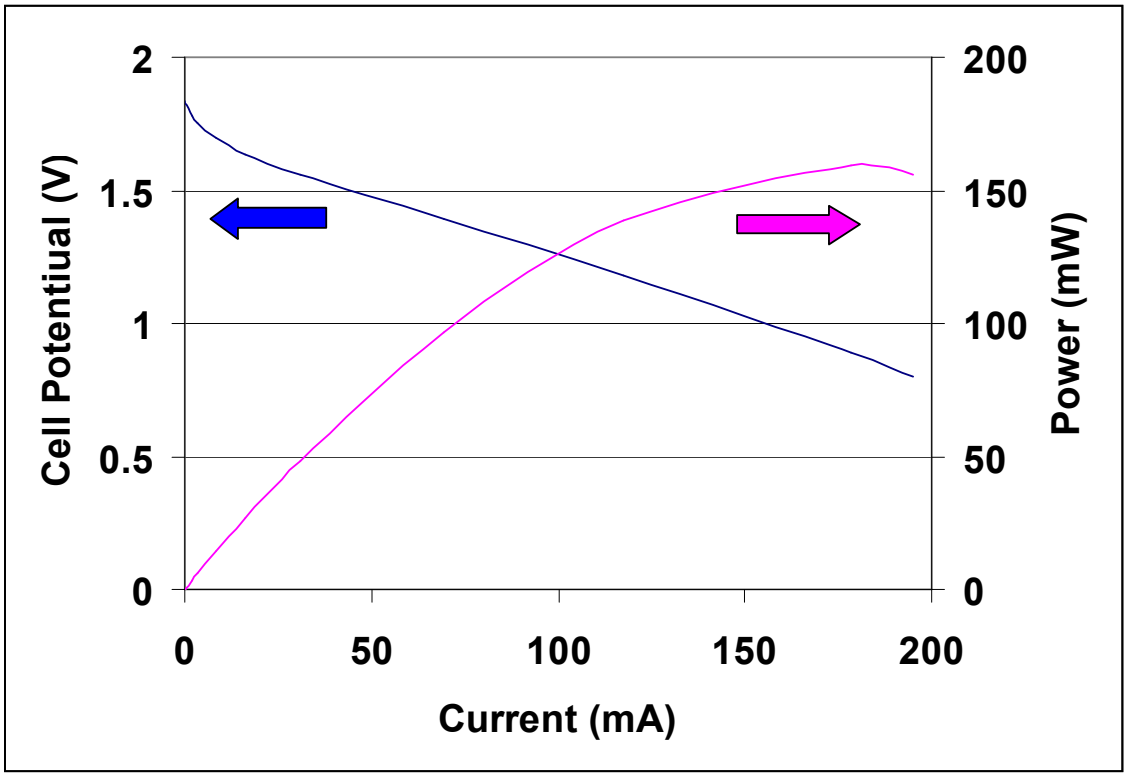

Fig. 2.18: Polarization data for the AA MFC with LAH fuel

Activation and Ohmic contributions to polarization are clearly visible in Fig. 2.18, however the increasingly negative slope at high current which indicates concentration polarization, is largely absent. This occurs because the maximum current density in water recycling MFCs is limited by the water transport in the MEA, not oxygen transport to the cathode or hydrogen transport to the anode, as in conventional fuel cells operating at high current. Once the water transport limit is reached in a water recycling MFC, further increases in the load serve only to reduce the cell potential.

The data presented in Fig. 2.18 were taken at the beginning of the discharge of a fresh MFC, and changes throughout discharge as the mass transfer resistance in the fuel

increases. The long-term performance of the MFC under constant current and constant potential discharge tests shows these changes, and is presented in Chapter 4.

Chapter 3: Self Regulating Hydrogen Generator

Chemical hydrides have received considerable attention since their initial synthesis in the 1940s, as promising fuels for MFCs due to their superior hydrogen storage density relative to conventional hydrogen storage methods (e.g. compressed gas in cylinder) [3.1, 3.2]. Although several mechanisms for releasing hydrogen from chemical hydrides have been explored, including thermal decomposition (thermolysis) and the water-hydride (hydrolysis) reaction, hydrolysis appears to be the most promising due its high hydrogen storage density, controllability, high practical yield, and compatibility with water recycling fuel cells. Recent studies of hydride hydrolysis reactions with water vapor (vs. past studies with liquid water) have demonstrated improved yields (approaching unity) at rates sufficient for MFCs [3.3-3.5]. This chapter explores the chemistry of the hydrolysis reaction, hydride selection and evaluation, the impact of hydride particle size and void fraction on hydride reaction rate and yield, and the development of self-regulating hydrogen generator utilizing a pneumatic valve to regulate the hydrolysis reaction (hydrogen generation) rate in a AA MFC.

3.1 Hydrogen Generator Design

The hydrogen generator (Fig 3.1) comprises an engineered chemical hydride fuel pellet packed inside of a pneumatic valve. The fuel pellet formulation (chemistry, particle size, void fraction, geometry) is engineered to maximize delivered energy while meeting the minimum hydrogen generation rate (i.e. power) requirements of the AA, as described

below. The pneumatic valve (valve diaphragm, moving valve, stationary valve) controls the hydrogen generation rate (hydrolysis reaction rate) by modulating the conductance path between the fuel cell (water source) and hydride fuel, based on the pressure difference (ambient minus internal) across the valve diaphragm.

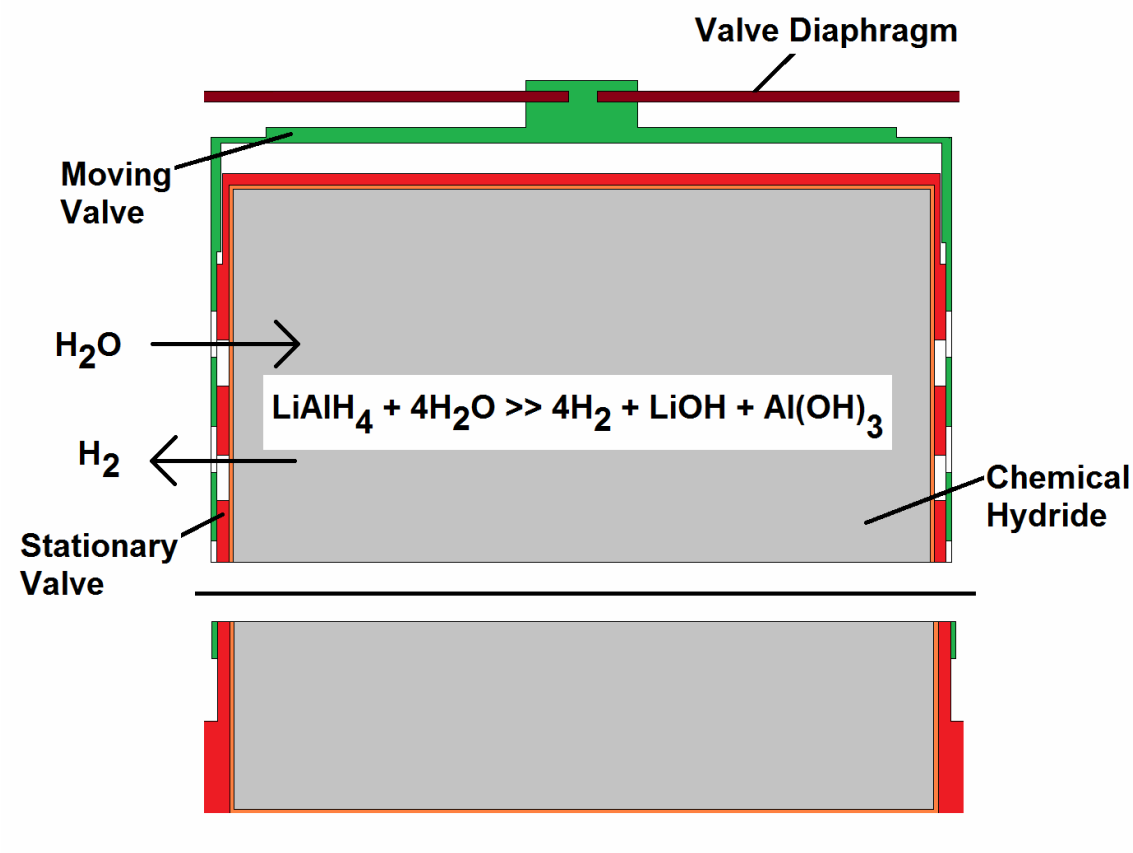

Fig 3.1: Hydrogen generator schematic

When an electrical load is placed on the MFC, hydrogen is consumed by the fuel cell, causing the internal pressure to drop and the diaphragm to deflect inward. This inward deflection opens the valve and allows water vapor to diffuse to and react with the hydride, generating hydrogen. When the load is removed hydrogen consumption stops

while hydrogen generation continues, causing the internal pressure to rise and the diaphragm to deflect outward. This outward deflection closes the valve and stops water vapor transport to the hydride and hydrogen generation. The valve is partially open under normal operating conditions; it closes or opens completely under no-load or maximum-load conditions, respectively.

A range of design parameters were considered for each of the hydrogen generator components (pneumatic valve, fuel pellet). The design parameters, range tested, selected values, and rational are summarized in Table 3.1. A detailed discussion of the pneumatic valve and fuel pellet design parameters is presented below.

Table 3.1: Parameters for hydrogen generator design

	Design Parameter	Range Tested	Selected Value	Rational
Pneumatic Valve	Diaphragm material	Stainless steel and PET	PET	Achieves desired deflection within pressure range
	Diaphragm thickness (μm)	12 to 100	100	Achieves desired deflection within pressure range, minimizes H2 permeation losses
	Diaphragm travel (μm)	150 to 800	600	Achieves desired valve conductance
	Valve open fraction (%)	10 to 45	35	Good tradeoff between closed leak rate and open conductance
	Stationary/movable overlap (μm)	100 to 500	200	Good tradeoff between closed leak rate and open conductance
	Lubricant	None, Light machine oil	Light machine oil	Reduces friction and improves closed leak rate
	Stationary valve wall thickness (μm)	100 to 500	500	Minimum thickness to contain fuel pellet expansion
	Moveable valve wall thickness (μm)	50 to 200	100	Lower limit of fabrication feasibility
	Stationary valve material	PET, stainless steel	Stainless steel	Need strength to contain fuel pellet expansion
	Moveable valve material	PET, stainless steel, brass	Brass	Prevents binding, reduces friction between stationary/moveable valve
Fuel Pellet	Chemistry	LiH, CaH2, LiAlH4, NaAlH4	LiAlH4	Highest practical energy density
	Particle size (μm)	Polydisperse: <20 to 250 Monodisperse: 5, 20, 50	Monodisperse: 5	Optimal value to minimize mass transfer resistance in fuel pellet
	Initial void fraction (%)	43 ,71, 86	43	Lowest tested value, lower may be better for low-power applications
	Geometry	Cylindrical, annular	Cylindrical	Reduces pellet fabrication complexity, increases energy density. Annular pellets don't significantly increase rate

3.2 Chemical Hydride Hydrolysis

In hydrolysis reactions, hydrogen is release from the chemical hydride via an irreversible and exothermic reaction with water. Simple hydrides react with water according to:

Simple hydride hydrolysis: $$MH_n + (n+x)H_2O = M(OH)_n \cdot xH_2O + nH_2 \qquad (3.1)$$

where M is a metal of valence n, and x is structural water of crystallization. The value of x can range from zero to greater than 20 depending on the specific hydride and the conditions under which the reaction is carried out. Complex hydrides react according to:

Complex hydrolysis: $$M(M'H_4)_n + (2n+x)H_2O = M(M'O_2)_n \cdot xH_2O + 4_nH_2 \qquad (3.2)$$

where n is the valence of the metal M, M′ is an element from group IIIA of the periodic table, such as boron or aluminum, and x is structural water of crystallization. Equation (3.2) is written with the assumption that the reaction has been carried out under conditions that produce a dry solid and dry gas; in this case the solid phase product is best described as a hydrated mixed metal oxide. As with simple chemical hydrides, the reaction products near ambient conditions are hydroxides, not oxides, and since the structure of the M′ hydroxide depends on the metal, there is no compact way to express this reaction under these conditions.

Hydrolysis reactions that occur under near-ambient conditions with liquid water tend to produce higher values of x, while reactions with water vapor tend to produce lower values. For example, the hydrolysis of $LiAlH_4$ occurs via the following reaction:

$$LiAlH_4 + (4+x)H_2O = LiOH \cdot xH_2O + Al(OH)_3 + 4H_2 \qquad (3.3)$$

If the reaction is conducted with liquid water, computational studies suggest that up to seven water molecules (x=7) can hydrate $LiOH$ under certain conditions, although only the monohydrate (x=1) has been confirmed by experiment [3.6]. However, if the reaction is conducted with water vapor, the value of x will be zero if the water activity (relative humidity) in the reaction products is below 0.2 [3.7]. Maintaining x as close to zero as possible is critical to achieving high performance in MFCs for the following reasons:

- Required for water balance (i.e. 1 mol of water produces 1 mol of hydrogen)
- Maintains higher reaction rates by preventing hydrated hydroxide from building up on surface of unreacted hydride particles
- Maintains higher reaction yield by preventing reaction product expansion due to hydrated hydroxide formation in reaction products.

These reasons as well as several others are described in section 3.3.

3.3 Chemical Hydride Selection and Evaluation

3.3.1 Hydride Selection

Candidate hydrides were selected for preliminary experiments from the group of simple and complex hydrides identified by Kong et al. [3.3] by applying the selection criteria given by MacPherson [3.10]. These criteria include (1) maximum deliverable hydrogen, (2) ambient state and density, (3) storability, (4) delivery manageability and controllability of the reaction, (5) availability of the parent elements, (6) environmental impact, (7) recycleability, (8) heat of reaction, and (9) potential for economic feasibility.

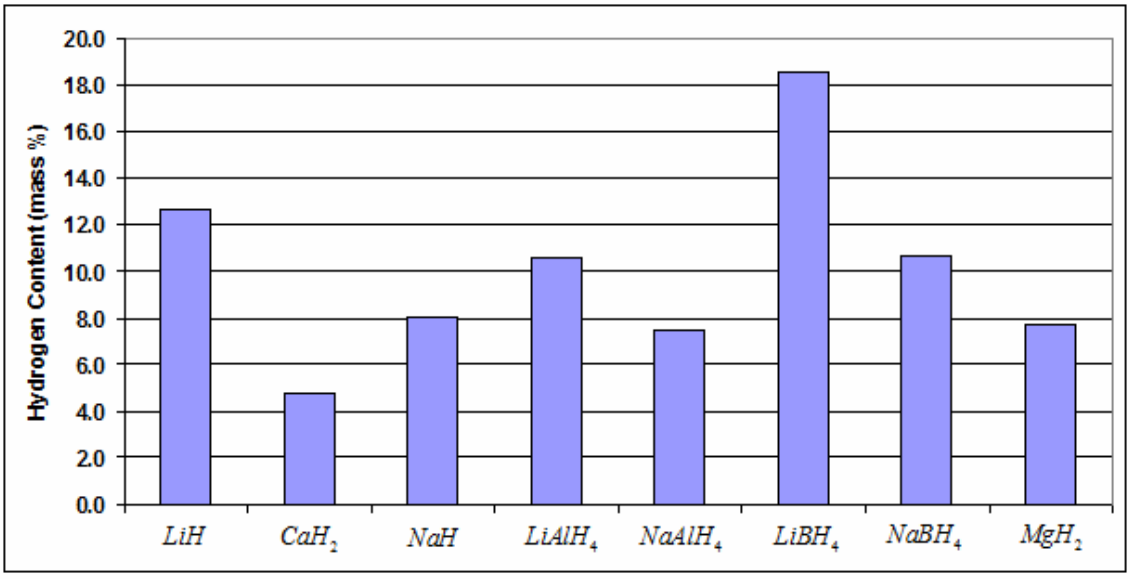

Fig 3.2. Simple and complex hydrides and their formula hydrogen content selected for evaluation by Kong et al. by applying MacPherson's criteria

Starting with the hydrides selected by Kong et al. based on MacPherson's criteria (Fig 3.2), we narrow the list further by applying three additional requirements: (1) hydrogen release must occur via a hydrolysis reaction at near room temperature; (2) the hydride must react with water vapor; (3) the hydrolysis reaction must produce one mol of hydrogen per mol of water vapor consumed.

MgH_2 is eliminated because it does not react fast enough with water under normal ambient conditions due to formation of a $Mg(OH)_2$ surface layer which slows water transport to the un-reacted core [3.10]. The borohydrides ($LiBH_4$ and $NaBH_4$) are eliminated because they do not react directly with water vapor [3.8]. The remaining four hydrides in Fig 3.2 meet the additional criteria described above, and are selected for preliminary experiments. Table 3.2 contains the reaction equation, reactant and product energy density values for these four hydrides.

Table 3.2: Reaction, reactant and product energy density, for hydrides meeting the selection criteria

Hydride	Reaction	Formula H2 Content (mass %)	Specific Energy (Whr/kg)	Reactant Energy Density (Whr/l)	Product Energy Density (Whr/l)
LiH	LiH + H2O >> H2 + LiOH	12.7	4726	3875	2366
CaH2	CaH2 + 2H2O >> 2H2 + Ca(OH)2	4.8	1783	3031	2238
LiAlH4	LiAlH4 + 4H2O >> 4H2 + LiOH + Al(OH)3	10.6	3954	3626	3103
NaAlH4	NaAlH4 + 4H2O >> 4H2 + NaOH + Al(OH)3	7.5	2779	2515	2927

The reactant energy density values in Table 3.1 are calculated based on the energy content and volume of the hydride. The product energy density values are calculated based on the energy content of the hydride and volume of the hydride reaction products. For both parameters, the volume of water is neglected, as it is assumed that the water is recovered from the fuel cell. The energy values are calculated assuming 1) stoichiometric

reactions as shown in Table 3.2, 2) hydrogen is converted to electrical energy in a PEM fuel cell operating at 0.6 V, 3) all other sources of inefficiencies and losses are negligible.

Product energy density is included in the analysis because all of the hydrides in Table 3.2 (except $NaAlH_4$) have smaller product than reactant energy densities. A smaller product energy density implies that the volume of the hydride is smaller than that of its reaction products, thus additional void space is required in the hydride to accommodate reaction product expansion. In volume-constrained applications (as is the case with the portable devices in which MFCs are used), this reduces the energy density of the hydride to that of its fully expanded reaction products. Thus, the smaller of the reactant or product energy densities is selected as the relevant basis of comparison.

3.3.2 Hydride Evaluation

Samples of the hydrides in Table 3.2 are reacted in a vapor-hydrolysis reactor as described below. Based on the reaction yields observed in these experiments and the theoretical reactant and product energy density values (Table 3.2), we determine that $LiAlH_4$ has the highest practical energy density, and select it for further experiments to explore the effects of void fraction and particle size on reaction rate and yield.

Our selection of $LiAlH_4$ is somewhat surprising given the findings of Kong et al., who selected CaH_2 and LiH based on a similar analysis. A discussion of this discrepancy and a hypothesis for the differing results are presented below.

3.3.3 Hydride Processing

The hydrides selected for testing were purchased from the Sigma Aldrich Chemical Company. Their catalog number, purity, and forms are summarized in Table 3.3.

Table 3.3: Form, purity, and catalog numbers for selected hydrides

Hydride	Form	Purity (%)	Catalog Number
LiH	Powder	95	201049
CaH2	Powder	95	208027
LiAlH4	Powder	97	62420
NaAlH4	Powder	93	685984

The raw hydride powders were processed to three sizes (5 μm, 20 μm, and 50 μm diameters) using a jet mill (Jet Pulverizer Co, Moorestown, NJ). Jet milling was chosen for processing the hydrides because it is capable of producing very small particles with narrow size distributions, while avoiding the excess heat production (which can decompose the hydride) and contamination that are typically associated with traditional milling processes (e.g. ball milling) [3.9].

For the hydride candidate selection tests, ~0.5 g of hydride (5 μm size distribution) was loosely packed by hand into the fuel chamber, leaving sufficient free volume for reaction product expansion. The purpose of the selection tests was to determine the reaction yield, unconstrained by particle size or reaction product expansion (void fraction) limitations.

For all subsequent tests with the down-selected hydride ($LiAlH_4$), a hydraulic press (Carver, Wabash, IN) was used to compress the hydride to the desired void fraction. The desired mass of hydride for each test was divided in ten equal parts and pressed in stages,

to minimize density gradients within the fuel pellet. Depending on the desired mass of hydride in the test, a force of up to 4000 lbs (~23000 psi) was required to compress the hydride. Tests were performed with three particle size distributions (5 μm, 20 μm, and 50 μm diameters) and at three initial void fractions (86%, 71%, 43%).

3.3.4 Hydrolysis Reactor

A water-vapor-hydrolysis reactor was constructed as shown in Fig. 3.3, and it is similar in design to the reactor described by Kong et al. [3.3]. The reactor chamber is constructed from stainless steel and is hermetically sealed during operation. Hydrogen generated by the hydrolysis reaction is trapped inside the reactor, causing the pressure to rise over time. The reaction rate and yield are determined based on the rate of pressure rise and final pressure in the reactor, respectively.

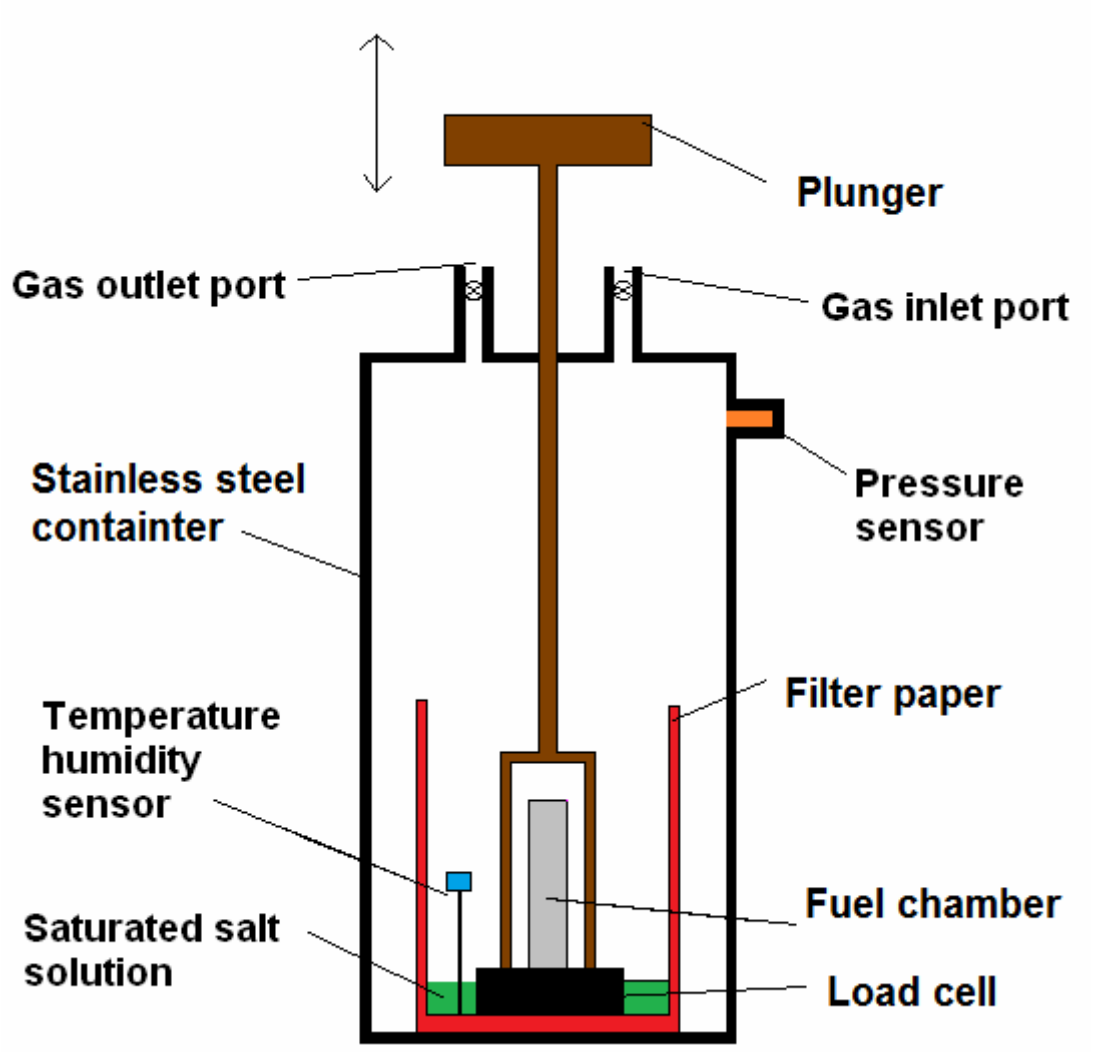

Fig. 3.3: Cross-section schematic of the vapor hydrolysis reactor

The hydride is contained in a cylindrical fuel chamber constructed from perforated stainless steel tubing. The fuel chamber is positioned on a load cell (Futek, Irvine, CA) above a pool of saturated salt solution. Filter paper soaked in the saturated salt solution and supported by a stainless steel screen surrounds the fuel chamber. The saturated salt solution (a slush comprised of magnesium nitrate and distilled water) maintains a constant humidity boundary (nominally ~54.4% at 20ºC) around the fuel chamber.

Excess water is provided to maintain constant humidity throughout the test. The load cell measures the mass of the hydride vs. time. The data is used to monitor reaction stoichiometry and water uptake by the reaction products.

The fuel chamber is weighed before and after filling with hydride. The exact mass of hydride loaded in the fuel chamber is determined by subtracting the empty mass of the fuel chamber from its fully loaded mass. All masses are measured with an analytical balance (Ohaus, Parsippany, NJ).

A temperature and humidity sensor (Sensiron, Los Angeles, CA) positioned between the filter paper and the fuel chamber monitors the temperature and humidity in the chamber. Similarly, a pressure sensor (Honeywell, Morristown, NJ) positioned near the top of the chamber monitors the pressure in the chamber. A movable plunger covers the fuel chamber and seals it from the surrounding environment during setup. The plunger is raised at the start of the test, allowing water vapor access to the fuel chamber.

The fuel chamber is packed with hydride inside a nitrogen-purged dry box and transported to the reactor in a sealed container. The fuel chamber is placed in the reactor and quickly covered with the plunger, to prevent the hydride from reacting with atmospheric water vapor while the reactor is assembled and purged. Once assembled, the reactor is purged with hydrogen for 30 minutes at 1000 sccm flow rate to eliminate atmospheric gases.

All experiments are carried out at 20ºC and 54.4% relative humidity. The pressure in the reactor starts at 1 atm, ultimately rising to 2-4 atm (depending on the mass and chemistry

of the hydride) at the end of the test. Reaction rate and yield are calculated based on the rate of pressure rise and final pressure in the reactor, respectively.

3.3.5 Hydride Candidate Evaluation

The four down-selected hydrides (Table 3.3) were tested in the hydrolysis reactor, and their hydrogen production profiles are shown in Fig 3.4.

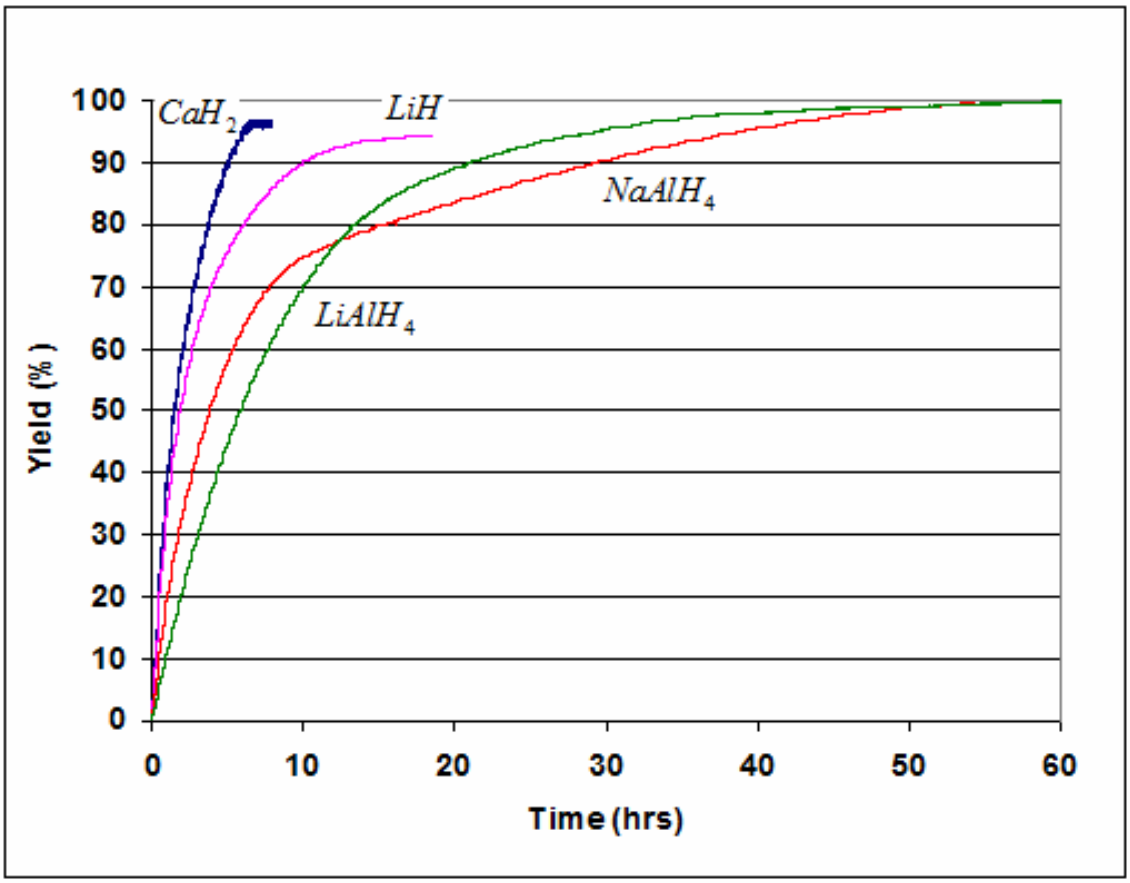

Fig 3.4: Hydrogen production profiles for vapor hydrolysis reactions with candidate hydrides

High reaction yields were observed for all four hydrides, with CaH_2 and LiH achieving 96% and 94% yield respectively, and $LiAlH_4$ and $NaAlH_4$ both achieving ~100% yield. Reaction yields and practical energy density values for the four candidate hydrides are shown in Table 3.3. Yields are calculated based on the pressure rise in the reactor, and the reaction equations listed in Table 3.4, assuming complete (stoichiometric) reactions. Practical energy density is calculated for each hydride by taking the smaller of its reactant or product energy density and multiplying it by its reaction yield. Based on this analysis, $LiAlH_4$ has the highest practical energy density of the four hydrides.

Table 3.4: Reaction, reactant and product theoretical energy density, reaction yield, and practical energy density for candidate hydrides

Hydride	Reaction	Reactant Energy Density (Whr/l)	Product Energy Density (Whr/l)	Reaction Yield (%)	Practical Energy Density (Whr/l)
LiH	LiH + H2O >> H2 + LiOH	3875	2366	94	2224
CaH2	CaH2 + 2H2O >> 2H2 + Ca(OH)2	3031	2238	96	2149
LiAlH4	LiAlH4 + 4H2O >> 4H2 + LiOH + Al(OH)3	3626	3103	100	3103
NaAlH4	NaAlH4 + 4H2O >> 4H2 + NaOH + Al(OH)3	2515	2927	100	2515

The high observed reaction yields for all four candidate hydrides is surprising for two reasons. First, for all of the hydrides except LiH, yields are higher than the minimum purity (Table 3.3) specified by the manufacturer, indicating that the hydrides samples in our tests are very nearly pure. Second, we expected lower yields from $LiAlH_4$ and $NaAlH_4$ (~73% and ~49%, respectively) based on the results reported by Kong et al., however the yields for both reactions were ~100% [3.3].

We hypothesize that the yields we observed are higher for two reasons: First, we use jet-milled hydrides with uniform and small (5 μm) particles, as opposed to the larger particle size and broad size distribution as-delivered by the manufacturer (Fig 3.5) and used by Kong et al. in their experiments. The lower yields reported by Kong et al. may be a result of un-reacted hydride remaining in the core of the larger particles.

Second, we use small hydride samples (~0.5 g) in our tests, and provide ample volume in the fuel chamber for reaction product expansion, resulting in reaction products that are dry, free-flowing, and non-agglomerated. This is opposed to reaction products described by Kong et al. as "hard solid masses," which may have limited yield by preventing water vapor from accessing unreacted hydride in the interior of the pellet [3.3].

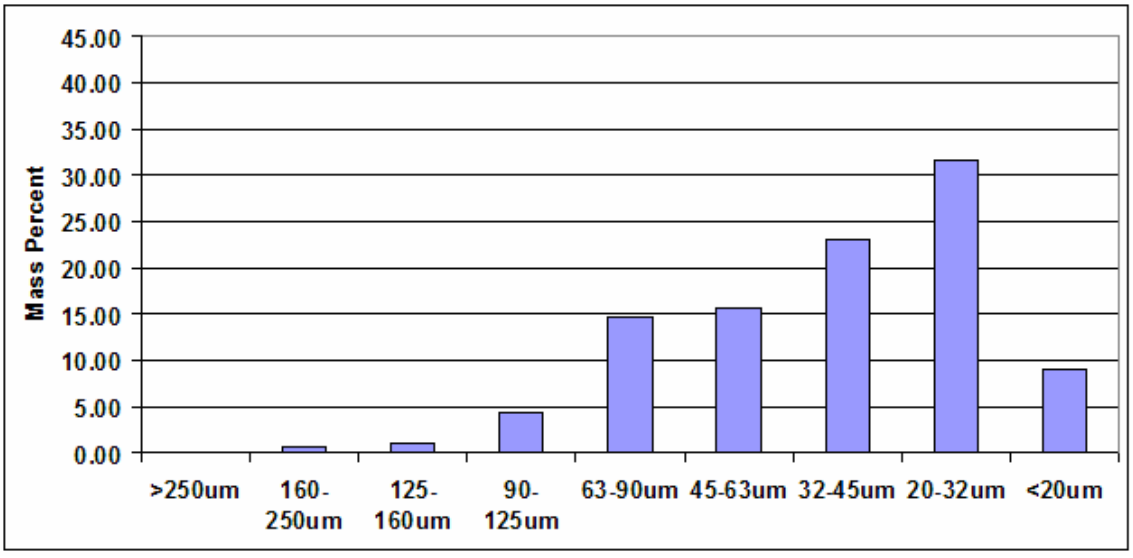

Fig 3.5: Particle size distribution for $LiAlH_4$ as-received from the manufacturer

Hydrogen generation rates for the candidate hydrides in the (initial) linear region range from 1e-5 mol sec^{-1} for CaH_2 to 3.5e-6 mol sec^{-1} for $LiAlH_4$, corresponding to 1.2 W to 0.4 W equivalent power, respectively, assuming that the hydrogen is converted to electricity in a fuel cell operating at 0.6 V. Reaction rates for all four candidate hydrides are adequate for the MFC, which has a power target of 0.15 W.

Based on the practical energy density and initial reaction rates, $LiAlH_4$ is selected for further experiments to explore the effects of void fraction and particle size on reaction rate and yield.

3.3.6 Particle Size Effects

Hydrolysis reactions with $LiAlH_4$ were repeated at three particle sizes (5 μm, 20 μm, 50 μm diameters) at an 86% initial void fraction (Fig. 3.6).

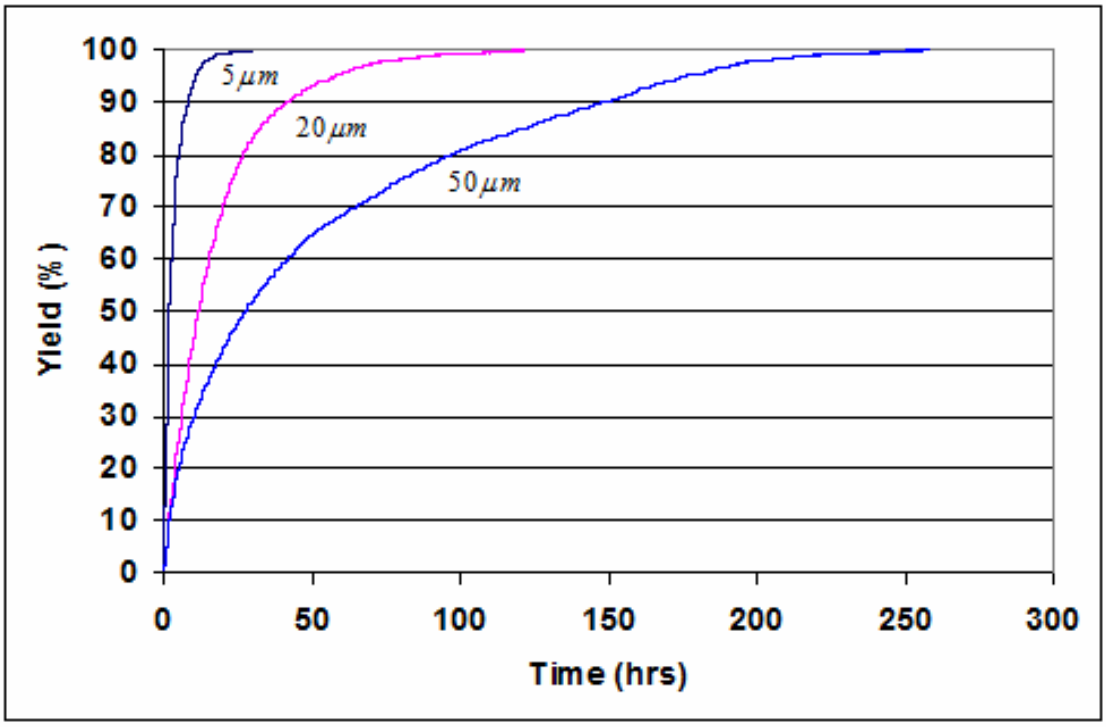

Fig 3.6: Effects of particle size (5 µm, 20 µm, 50 µm) on reaction rate and yield in the hydrolysis reactor, at 86% initial void fraction

The tests were conducted at a high initial void fraction (86%) to minimize the impact of reaction product expansion on reaction rate and yield. The reaction yield for all three particle sizes was ~100%, indicating that particle size does not impact yield for the range of particle sizes tested. Reaction rates, however, were significantly impacted by particle size. Initial rates ranged from 3.5e-6 mol sec^{-1} for the 5 µm particle size, to 1.5e-6 mol sec^{-1} for the 50 µm particle size, corresponding to 0.4 W to 0.17 W, respectively.

The slower reaction rate of the 50 µm particle size would begin to limit the maximum power output of the MFC (peak power of 150 mW) after only a few hours, thus in order to minimize the impact of the decreasing reaction rate with time, a smaller particle size is preferred.

There is, however, a lower limit to the preferred particle size from several of perspectives. Fundamentally, as the particle size shrinks, so does the particle-to-particle spacing. Once this spacing becomes similar in magnitude to the mean free path of the gas, mass transfer rates begin to decrease as the transition from Fickian to Knudsen diffusion occurs. This transition occurs at ~1 μm particle size, for the conditions inside the MFC. In addition, current jet-mill technology has a lower particle size limit of ~0.5 μm, and has very low throughput at small particle sizes, impacting processing cost. Further, smaller particles are more reactive, and present a greater danger in case of an uncontrolled reaction with water. These factors must also be considered when selecting an optimal particle size for the MFC.

3.3.7 Void Fraction

Hydrolysis reactions with $LiAlH_4$ were repeated at three initial void fractions (86%, 71%, 43%) with 5 μm particles are shown in Fig 3.7.

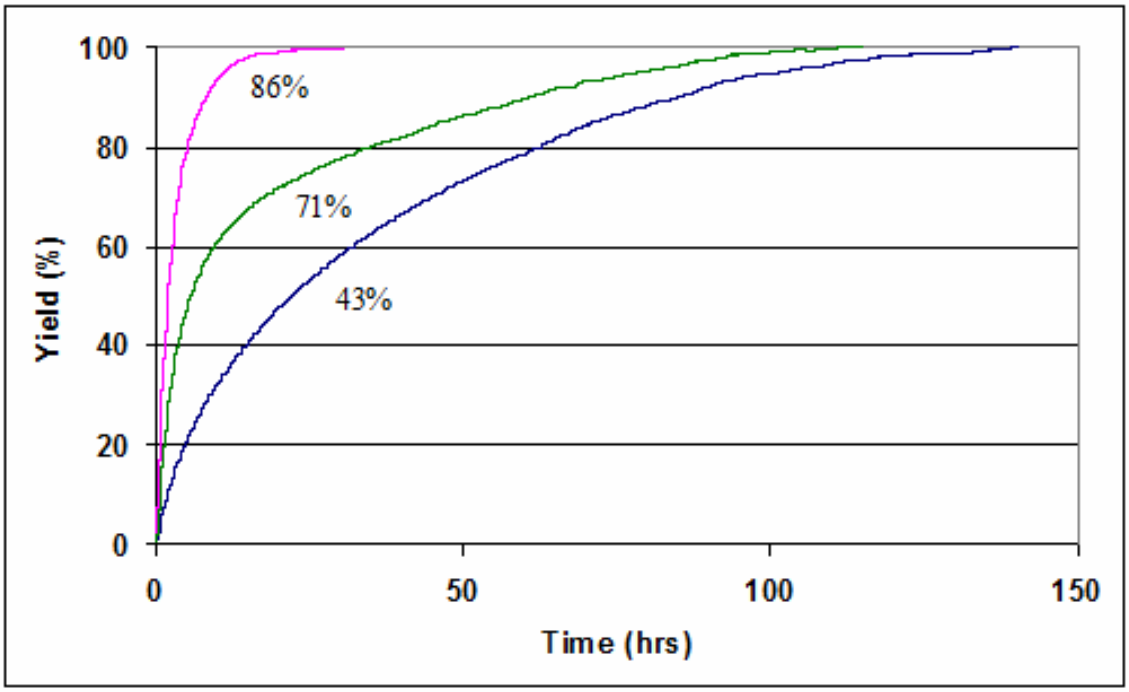

Fig 3.7: Effects of initial void fraction (86%, 71%, 43%) on reaction rate and yield for lithium aluminum hydride with 5µm particles

The tests were conducted using 5 µm particles to minimize the effect of particle size on reaction rate and yield. The reaction yield for all three particle sizes was ~100%, indicating that void fraction does not impact yield for the range tested. This is expected, as the calculated final void fraction for even the lowest initial void fraction test is 34%, after accounting for reaction product expansion. For all three tests, however, the actual final void fraction was significantly lower than the calculated value, as determined by the final mass of the reaction products as measured by the load cell. Figure 3.8 shows the actual and calculated mass of the reaction products for the test conducted at an 86% initial void fraction.

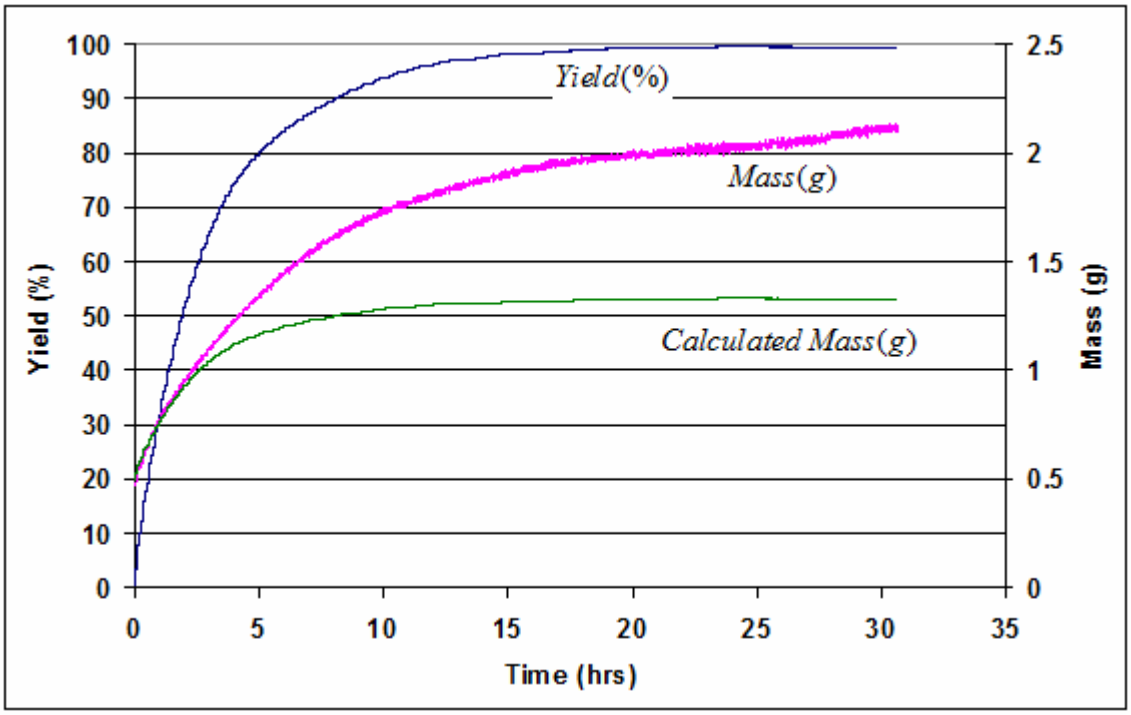

Fig 3.8: Measured and calculated mass of hydride plus reaction products vs. time for 5 µm particles at an 86% initial void fraction

The calculated mass is determined based on the measured yield assuming a stoichiometric reaction between $LiAlH_4$ and water vapor (Table 3.4). During the first few hours of the test, the calculated and actual masses are in good agreement, however, after three hours the masses begin to diverge, and the actual mass increased at a significantly higher rate than predicted by the reaction yield. The actual mass continues to rise even after the hydride reaction reaches completion.

Although there is no discussion in the literature of this phenomenon occurring for $LiAlH_4$, there is extensive literature concerning the LiH hydrolysis reaction, which also produces $LiOH$ as a reaction product. The work of Maupoix et al. demonstrates that

$LiOH$ will form lithium hydroxide hydrate ($LiOH \bullet H_2O$) under the conditions present in the fuel chamber (e.g. water activity >0.2), giving a plausible explanation for the higher mass accumulation rate and final mass of the reaction products [3.5]. Although beyond the scope of the current work, this side reaction, its impact on reaction rate and yield in MFCs will need to be considered when designing an optimal pellet configuration.

Reaction rates were significantly impacted by void fraction, although the exact effects are difficult to isolate given the confounding effects of the probable lithium hydroxide hydrate formation. Initial reaction rates ranged from 3.5e-6 mol sec^{-1} at 86% void fraction, to 3.3e-6 mol sec^{-1} at 43% void fraction, corresponding to 0.4 W to 0.38 W, respectively. A lower void fraction is desirable as it proportionally increases energy density; however it also decreases the reaction rate and likely increases lithium hydroxide hydrate formation. Further work will be required to understand the impact of initial void fraction and lithium hydroxide hydrate formation on reaction rate and energy density, and develop an optimal pellet configuration.

3.4 Diaphragm Valve

3.4.1 Valve Design

The diaphragm valve (Fig 3.1) comprises a flexible diaphragm, a moving valve, and a stationary valve. The moving valve is connected to center of the flexible diaphragm, coupling the movements in the flexible diaphragm (caused by changes in the differential pressure across the diaphragm) to the moving valve. The moving and stationary valves

have identical perforation patterns (slots) that are aligned when the valve is open (diaphragm fully deflected inwards), and misaligned when the valve is shut (diaphragm fully deflected outwards). The degree of alignment of the moving and stationary valves determines the conductance of the valve, and therefore the hydrogen generation rate. The moving and stationary valves in their open and closed positions are shown schematically in Fig. 3.9.

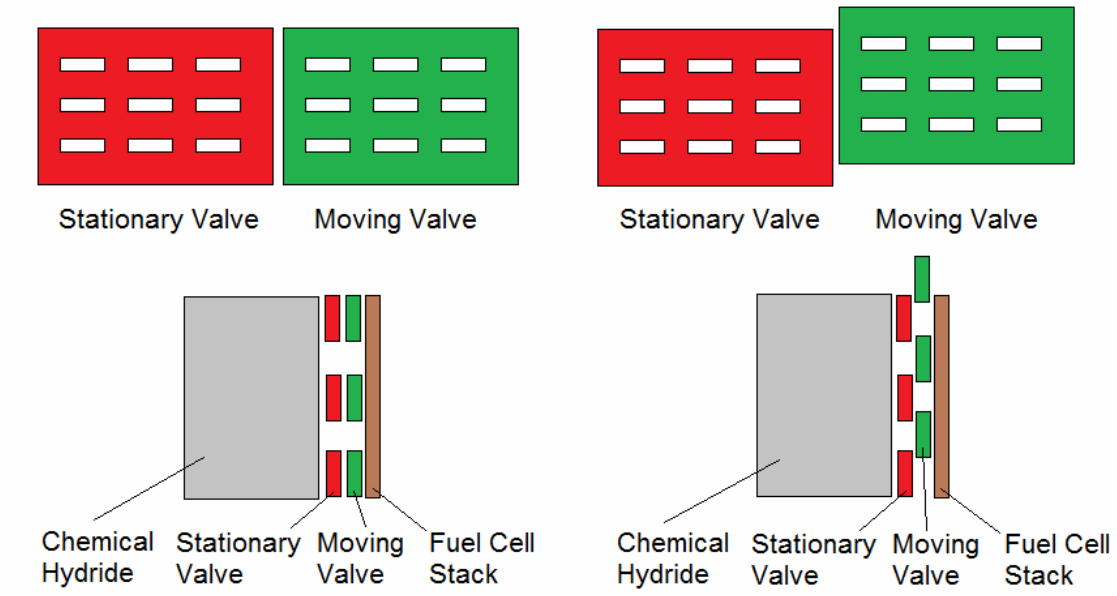

Fig. 3.9: Schematic of valve in open (left) and closed (right) positions. The position of the moving valve controls the conductance path between the fuel cell stack and the chemical hydride

The diaphragm is fabricated from 100 µm thick PET film (Fralock, Valencia, CA) using laser micromachining (Universal Laser Systems, Scottsdale, AZ). The moving and stationary valves are fabricated from brass and 316 stainless steel tubing, respectively, using conventional machining. A low viscosity oil lubricant (BP Lubricants, Baltimore

MD) is applied between the moving and stationary valves to reduce friction and to improve sealing. The center of the diaphragm is attached to the moving valve, and the perimeter of the diaphragm is attached to the anode support with an epoxy adhesive. The adhesive functions as a gas seal and mechanically holds the diaphragm in place.

3.4.2 Valve Characterization

The most important measures of valve performance in the AA MFC are the steady-state values of open and closed conductance, and the conductance as a function of the pressure difference across the diaphragm. The dynamic response of the valve is unimportant given the short mechanical time constant of the valve (large pressure forces and small moving mass) compared to the long pressure time constant (small hydrogen generation rate and large dead volume) of the MFC.

The open conductance of the valve determines the maximum power output of the MFC while the closed conductance determines the leak rate. If the closed conductance of the valve is too high (i.e, the leak rate is too high) the pressure in the system can rise to unsafe values, resulting in excessive hydrogen permeation losses through the PEM, or catastrophic failure of the MFC and rapid release of hydrogen. The MFC is stable if the hydrogen generation rate resulting from water vapor leakage through the valve is less than or equal to the hydrogen leak rate (primarily via permeation through the PEM). Per Chapter 2, this leak rate is typically on the order of $5E^{-9} molH_2 \sec^{-1}$, thus the maximum water vapor leak rate through the valve is also $5E^{-9} molH_2 \sec^{-1}$.

The open and closed conductance of the valve is determined indirectly—by monitoring the water vapor leak rate through the valve. From Fick's First Law assuming one dimensional diffusion (x direction):

Fick's First Law: $$J_x = -DA\frac{dC}{dx} \tag{3.1}$$

Where J_x is the mass transfer in the x direction, D is the diffusivity of water vapor in air, A is the area, and $\frac{dC}{dx}$ is the concentration gradient in the x direction. The valve conductance is the geometric constant relating the mass transfer to the concentration difference (ΔC) across the valve (Δx), thus rewriting Fick's First Law in terms of conductance (ρ):

Valve Conductance: $$\rho = \frac{A}{\Delta x} = \frac{J}{-D\Delta C} \tag{3.2}$$

Thus by measuring the mass transfer rate through the valve and the concentration difference across it, and the known value of the diffusivity of water vapor in air, the valve conductance can be determined and compared to the designed value. A test fixture was constructed (Fig 3.10) to determine the open and closed conductance of the valve.

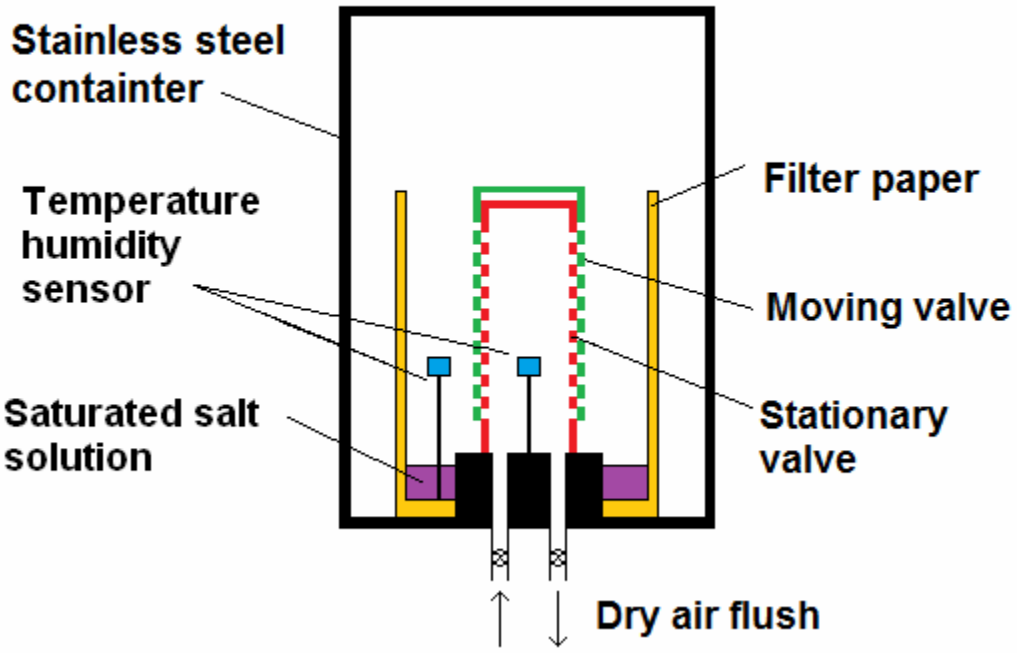

Fig 3.10: Schematic of test fixture for measuring valve conductance

The valve is enclosed in a sealed container and surrounded by filter paper which is soaked with a saturated salt solution to maintain a constant humidity boundary (potassium chloride, nominally 85.1% at 20ºC). Humidity sensors are positioned inside and outside of the valve. Ports connected to the inside of the valve are used to flush the interior with dry air.

Conductance tests are performed once the humidity inside and outside of the valve have stabilized. Once this has occurred, the two valves which are used to flush the inside of the valve with dry are closed, and the humidity is monitored over time. The humidity inside the valve rises over time, as water vapor leaks in from the humid exterior to the dry

interior of the valve. Fig 3.11 shows data from a closed valve conductance test. The leak rate of the valve (proportional to the slope of RH vs. time curve) at 50% delta RH (between the inside and outside of the valve) is $5.1E^{-10} molH_2 \sec^{-1}$, or ~ 10X lower than the value required for stability, as discussed above.

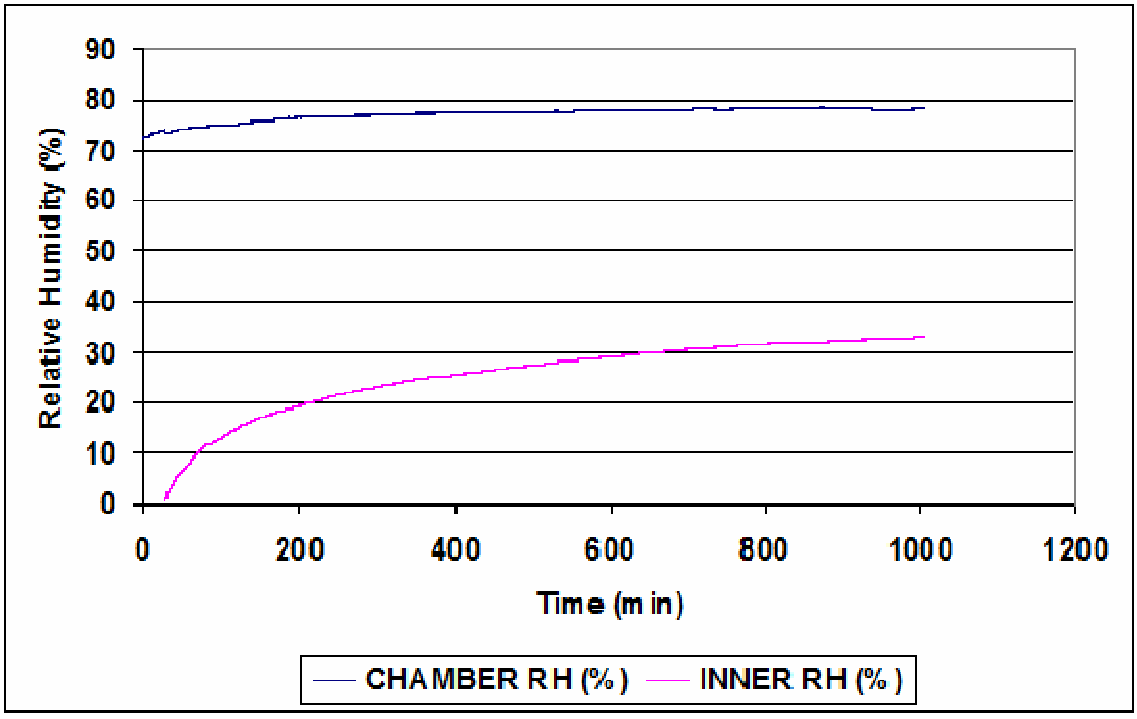

Fig 3.11: Data from a closed valve conductance test

Another important measure of valve performance is the deflection of the diaphragm as the pressure difference across it is varied, to verify that the valve fully opens and closes over the desired pressure range. The deflection of the valve diaphragm is measured using a laser micrometer (Keyence, Itasca, IL) as the pressure inside the MFC is varied between 6 and 18 psig (Fig 3.12).

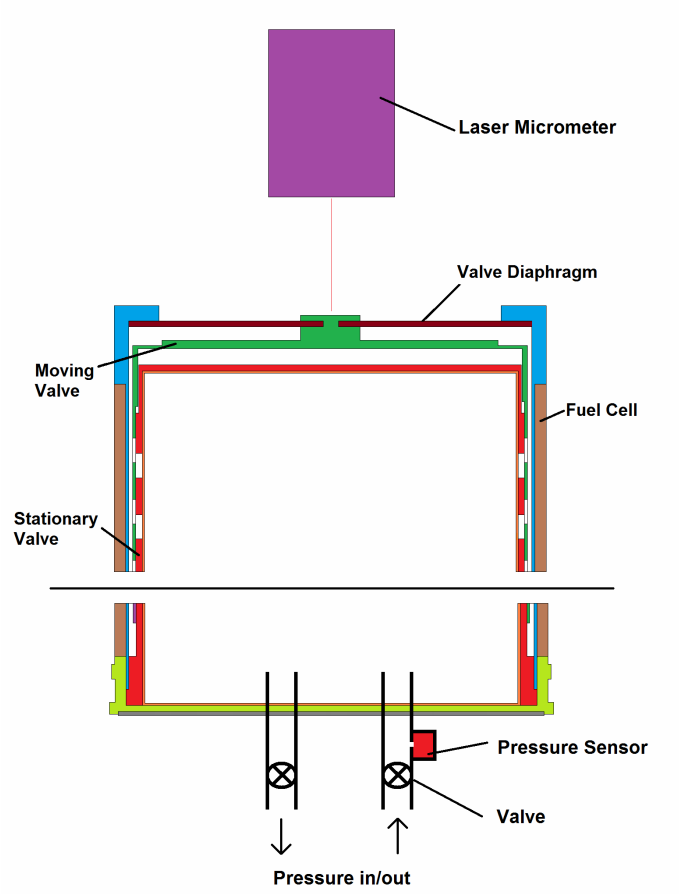

Fig 3.12: Schematic of test fixture for characterizing valve deflection vs. pressure

The valve is designed to be fully open at 6 psi and fully closed at 18 psi, and have a total travel of 600 μm. A typical valve performance curve for the MFC is shown in Fig 3.13. The numerical value of the starting and end points are arbitrary and determined by the initial distance between the valve diaphragm and the micrometer. Total travel is limited to 600 μm by stops built into the valve. The pressure inside the MFC is cycled between 6 and 18 psi; the valve diaphragm responds to the pressure change by moving

from its fully closed position (at -490 μm) to its fully open position (at 90 μm), and achieves a total travel of 580 μm, which is suitably close to the design value for the MFC to function properly.

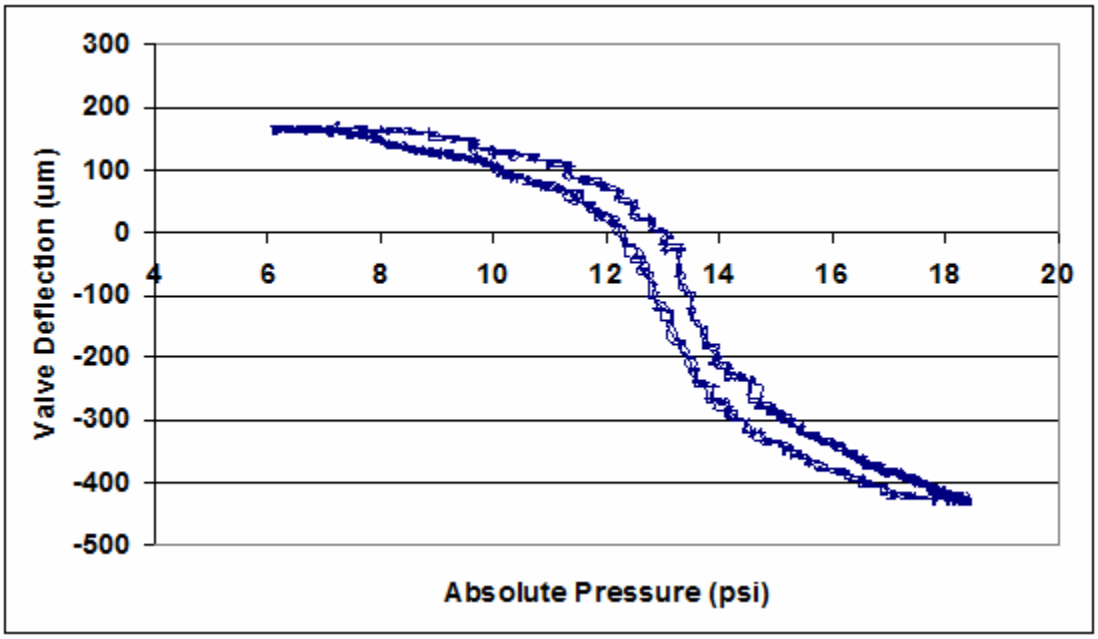

Fig. 3.13: Valve deflection vs. pressure for a single valve cycle (open to closed, closed to open)

A small amount of hysteresis is evident, due to friction between the fixed and moving valves; the resulting shift in operating pressure (typically < 1psi) does not significantly impact MFC performance. The valve performance is consistent over time, as the valve is cycled between its fully closed and fully open positions (Fig 3.14).

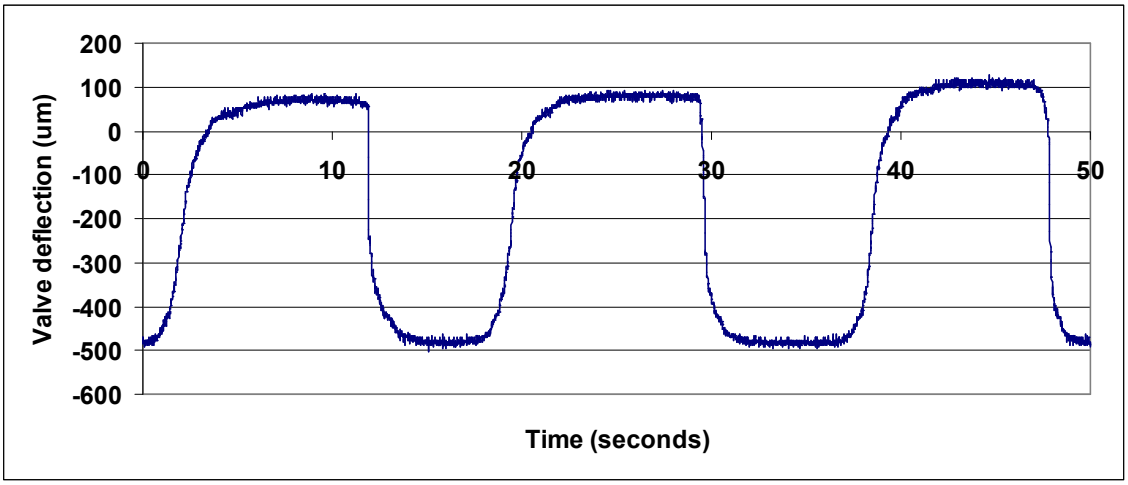

Fig. 3.14: Multiple valve deflection cycles, as the pressure in the MFC is varied from 6-18 psi

Chapter 4: Integrated AA Micro Fuel Cell

This chapter covers integration and characterization of the AA MFC. It begins with a discussion of the performance objectives and design parameters of the AA MFC, followed by a description of the AA design and operating principle. It continues with a discussion of the subassembly integration (fuel cell, hydrogen generator), and finishes with a discussion of the first and second generation device performance, using off the shelf and engineered fuel formulations, respectively.

4.1 Performance Objectives and Design Parameters

To be a viable replacement for AA batteries, the AA MFC must have similar electrical and physical characteristics, must be capable of operating in similar environments, must meet similar safety requirements, all while offering substantially longer runtime at a competitive cost. The present research is primarily focused on meeting the challenging electrical and physical requirements of AA batteries while providing longer runtime, and defers addressing the no-less challenging requirements of environmental range, safety, and cost to future work.

Among the most challenging aspects of replacing AA batteries in portable devices is the sheer variability in application requirements. Although standards exist for the configuration of AA battery "cavities" (e.g. geometry, diameter, height, terminal configuration) and for the safety tests they must pass, other parameters such as electrical load/duty cycle, and the physical arrangement (e.g. access to ambient air, thermal

characteristics) in the devices they power are equally important, but often unknown in advance to the battery designer. For example, batteries must work reasonably well in applications ranging from remote controls (low power consumption, intermittent operation) to digital cameras and flashlights (high power consumption, continuous operation). Meeting the requirements of a broad range of applications with very different operational requirements is extremely challenging.

The performance targets for the AA MFC (Table 4.1) are chosen to meet or exceed those of conventional AA batteries, which are designed to meet a broad range of application requirements. Some applications, however, such as those that have sealed battery cavities (e.g. waterproof) will be incompatible with the AA MFC, due to the inherent dependence of fuel cells on ambient air.

Table 4.1: Parameters and target values for the AA MFC design

	Design Parameter	Target Value	Rational
Electrical	Potential (V)	0.8 to 1.5	Meets potential requirements of majority of devices using AA batteries
	Peak Power (mW)	150	Meets power requirements of majority of devices using AA batteries
	Active Self Discharge (%/yr)	25	Provides resonable lifetime in majority of devices usiing AA batteries
	Shelf life (yrs)	10	Minimal discharge before activation
	Energy Density (Whr/l)	>1000	2-4X conventional AA batteries and state of the art micro fuel cells
Physical	Geometry	Cylindrical	Meets ANSI requirements for AA batteries
	Diameter (mm)	13.5 to 14.5	Meets ANSI requirements for AA batteries
	Length (mm)	50.1 (50.5 with terminal)	Meets ANSI requirements for AA batteries
	Terminal (mm)	0.4 height, 3 to 5 diameter	Meets ANSI requirements for AA batteries
Environment	Temperature Range (ºC)	0 to 40	Typical operating range for portable devices
	Humidity Range (% RH)	10 to 90	Typical operating range for portable devices
	Elevation (ft)	0 to 10000	Typical operating range for portable devices
	Safety	Consistent with AA primary batteries	Passes tests for AA primary batteries

4.2 Design and Operating Principle

The AA MFC (Fig. 4.1) has a 14mm diameter and 50.1 mm height, a volume of 7.7cc, and meets the ANSI physical requirements for AA batteries. It has a nominal operating potential ranging from 0.8V to 1.5 V (depending on electrical load) and has an

open circuit potential of ~1.9 V. Power output ranges from 0 to ~150mW, depending on the operating potential, state of discharge, and environmental conditions. The active self discharge (% loss in initial capacity per year) is less than 25% under nominal conditions (50% RH, 20ºC) but varies depending on the use case (load, duty cycle, environment). A shelf life of >10 years is projected based on hydrogen/water leakage into a hermetic package, but has not been verified experimentally. Energy density $>1000 Whrl^{-1}$ has been demonstrated in second generation prototypes, as described in section 4.5.

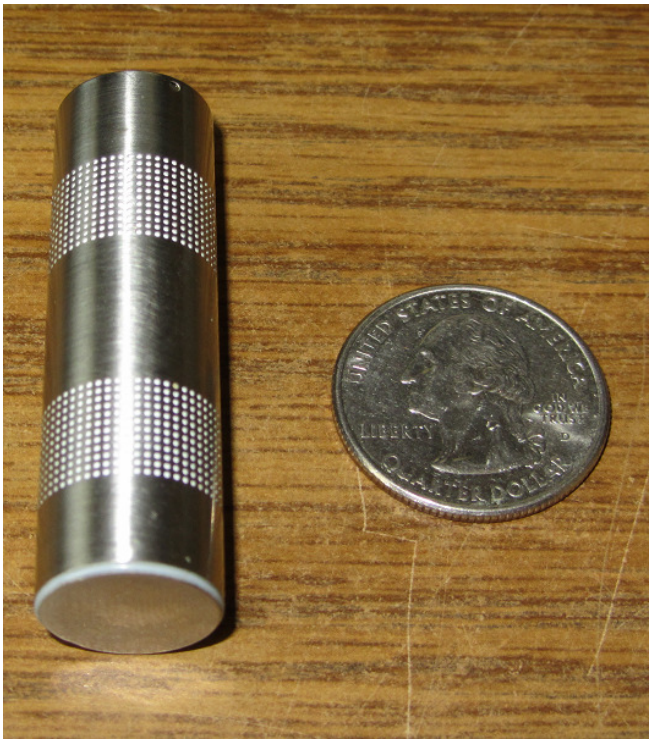

Fig. 4.1: Photograph of the MFC next to quarter for reference. Two perforated bands in the perimeter of the metal case provide air to the fuel cells. The cylindrical portion of the metal case is the cathode electrode, while the metal plate at the bottom is the anode electrode

The AA MFC (shown schematically in Fig 4.2) comprises a planar hydrogen-air PEM fuel cell integrated with a self-regulating hydrogen generator. Hydrogen is produced in the hydrogen generator via the hydrolysis reaction between a chemical hydride and water vapor. Hydrogen generated in the hydrogen generator and oxygen from ambient air react at the fuel cell, generating electrical energy, water vapor, and waste heat. Water vapor generated at the fuel cell cathode back-permeates through the PEM and diffuses to the hydride, where it reacts to generate additional hydrogen. The hydrogen generation process can be considered "water-less" in that it does not require an onboard water reservoir--all of the water required for the hydrogen generator is provided by the fuel cells and ambient air.

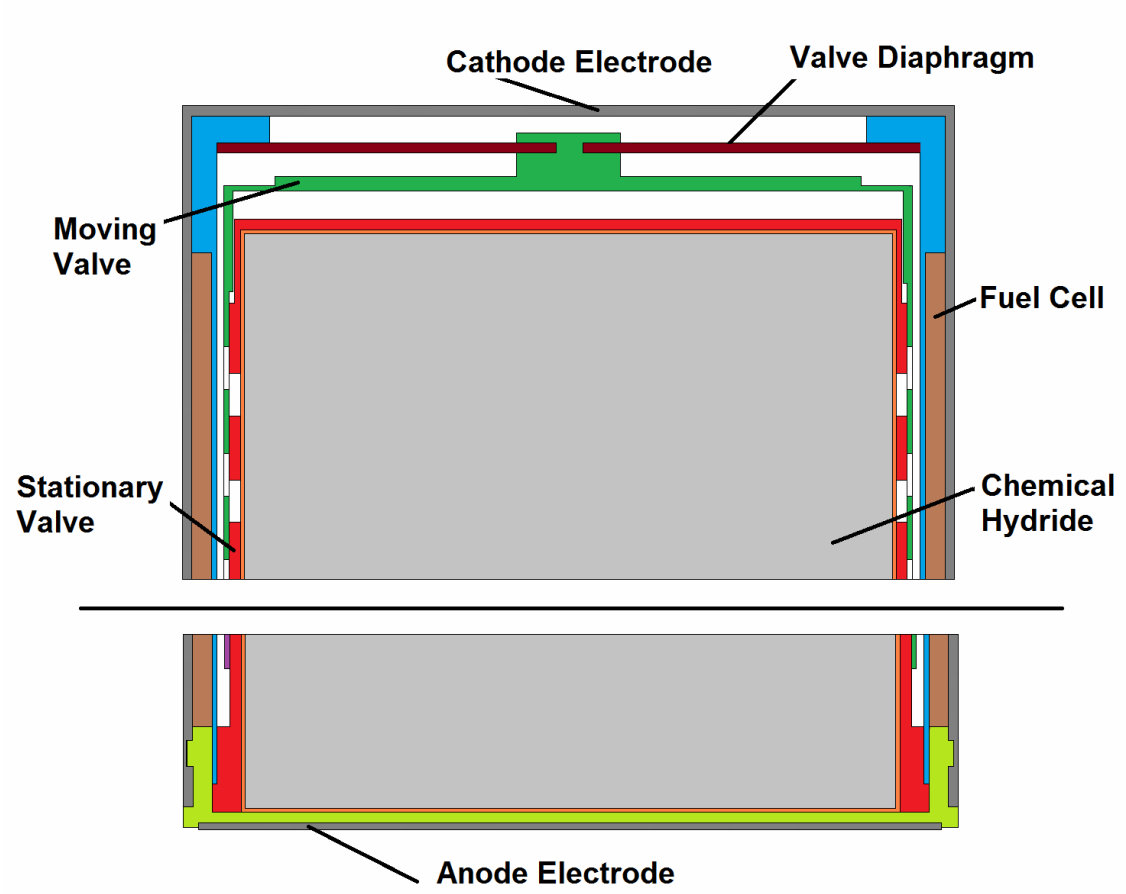

Fig. 4.2: Cross section schematic of the AA MFC. The middle portion of the MFC is removed to more clearly show the top and bottom

The hydrogen generation rate is regulated by a pneumatic diaphragm valve which controls diffusive transport of water vapor from the fuel cells to the chemical hydride, based on the position of the diaphragm. The position of the diaphragm is determined by the pressure difference (ambient minus internal) across it. When an electrical load is placed on the MFC, hydrogen is consumed by the fuel cell, causing the internal pressure to drop and the diaphragm to deflect inward. This inward deflection opens the valve and allows water vapor to diffuse to and react with the hydride, generating hydrogen. When

the load is removed hydrogen consumption stops, causing the internal pressure to rise and the diaphragm to deflect outward. This outward deflection closes the valve and prevents water vapor transport to the hydride and hydrogen generation. The valve is partially open under normal operating conditions; it closes or opens completely under no-load or maximum-load conditions, respectively.

4.3 Integration

A complete set of MFC components (not including the chemical hydride fuel pellet) is shown in Fig 4.3. The design and fabrication of the components, as well as the assembly and characterization of the planar fuel cell and hydrogen generator subassemblies are described in Chapters 2 and 3, respectively.

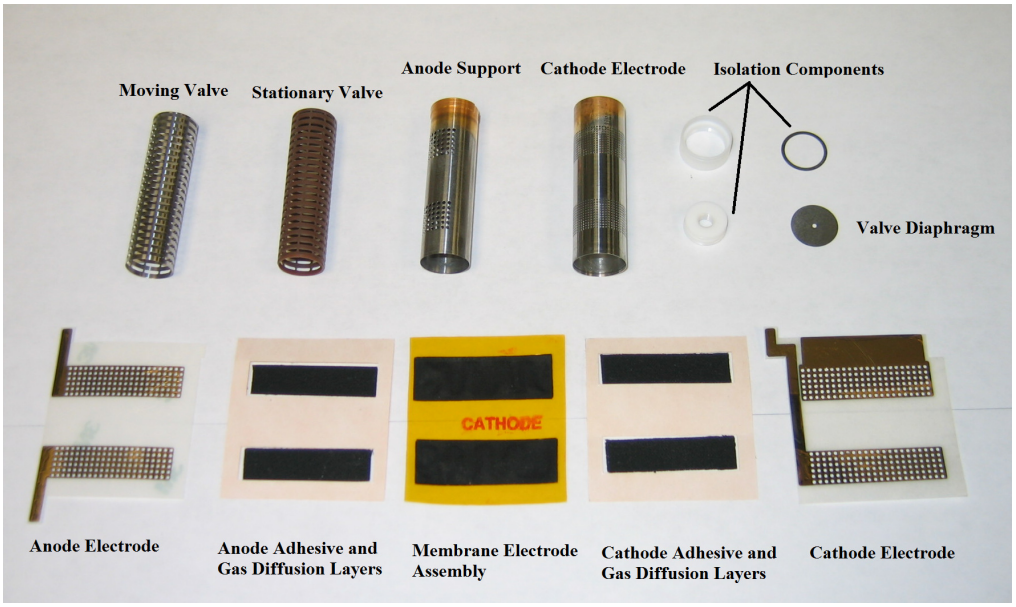

Fig 4.3: AA MFC components (not including the chemical hydride fuel pellet)

The integration and characterization sequence for the AA MFC are depicted in Fig 4.4. Step A) involves assembling the planar fuel cell (repeated here from Chapter 2), and is followed by electrical characterization (polarization and power) and leak tests with hydrogen, to verify electrical performance and seal integrity, respectively. Planar fuel cells that pass these tests are integrated (wrapped around) with the anode support, as depicted in step B).

In Step B, an adhesive layer on the back side of the planar fuel cell adheres it to the anode support, while an epoxy joint is created around the perimeter of the fuel cell to reinforce the adhesive seal. The anode support assembly is then subjected to the same electrical and leak tests as described in Step A), and those that pass move on to Step C).

In Step C) the valve (previously characterized for leak and actuation range, as described in Chapter 3) is integrated with the anode support assembly. Epoxy seals are formed between the diaphragm and anode support, diaphragm and moving valve, and fixed valve and anode support. The assembly is then tested for external (hydrogen) and internal (water vapor) leaks, and the actuation range verified; those that pass move on to Step D).

In Step D), the cathode electrode is integrated with the valve assembly. An epoxy seal is formed between the cathode electrode and the anode support. The completed MFC is then subjected to the same electrical, leak, and valve actuation test described above. Those that pass this final series of tests are fueled with LAH, sealed with epoxy, and are ready for final electrical characterization, as described in Chapter 3. The results of these tests are summarized below (Section 4.4 and 4.5).

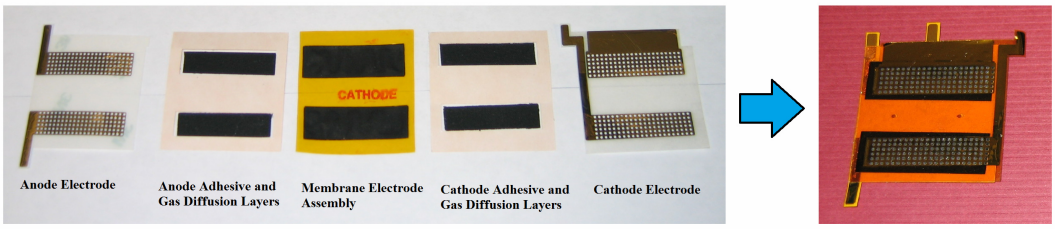

A) Planar fuel cell assembly
-Electrical characterization (hydrogen)
-Leak rate (hydrogen)

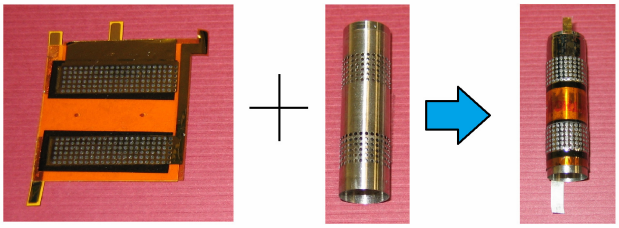

B) Anode support assembly
-Electrical characterization (hydrogen)
-Leak rate (hydrogen)

C) Valve assembly
-Leak rate (water vapor)
-Valve actuation

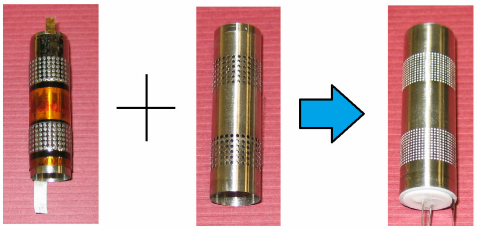

D) Cathode electrode assembly
-Electrical characterization (hydrogen)
-Leak rate (hydrogen)
-Valve actuation
-Electrical characterization ($LiAlH_4$)

Fig 4.4: AA MFC integration and test sequence

4.4 First Generation Micro Fuel Cell Performance

First generation AA MFCs were evaluated with 1.2V constant potential and 20mA constant current discharges, with two fuel formulations--roughly crushed tablets and packed powder, both with the particle size distribution as-received from the manufacturer and described in Chapter 3.

The LAH tablets had an initial density of $0.75 gcc^{-1}$, and were mechanically crushed into rough chunks of ~1-5mm diameter. The rough chunks and the residual powder were loosely packed by hand into the fuel chamber. A typical discharge curve for a MFC under 1.2V constant potential, using crushed LAH tablets, is depicted in Fig 4.5.

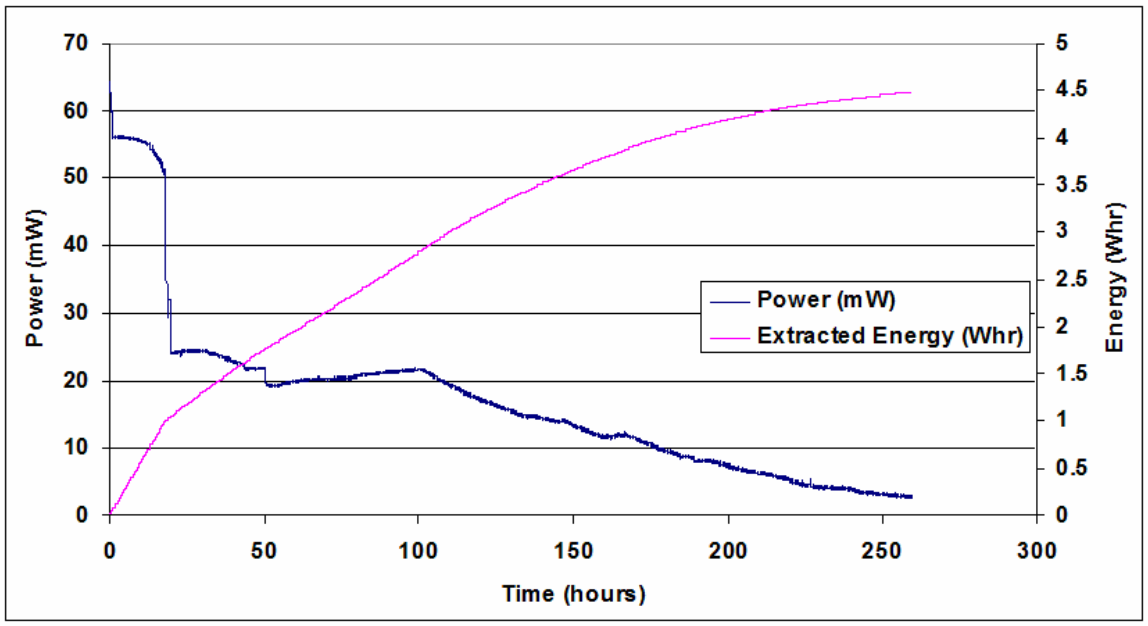

Fig 4.5: 1.2V constant potential discharge of first generation AA MFC fueled with 2.29g of crushed LAH tablets

The discharge curves for MFCs using crushed LAH tablets exhibit several common characteristics: 1) a short (few minute) initial period of higher power (60-70mW), likely caused by consumption of the initial charge of hydrogen in the fuel chamber 2) a longer period (10-20h) of slightly lower power (50-60mW), as the surface of the rough chunks and any powder in the fuel chamber is consumed 3) an even longer period (50-100h) of lower power (20-30mW) as the space between the large chunks is filled with expanding reaction products 4) the remainder of the discharge (150-200h) is marked by declining power (an exponential decay) as the void space between the particles is filled with expanding reaction products.

AA MFCs using crushed LAH exhibit low reaction yields, typically 50-60%. This is due to a significant amount of unreacted LAH remaining in the larger fuel particles at the end of the discharge, as confirmed by exposing the reaction products to liquid water following discharge in the MFC. The data in Fig 4.5 was taken for a AA MFC under 1.2V constant potential discharge, and filled with 2.29g of LAH. The MFC delivered 4.65Whr of electrical energy (of 7.75Whr theoretically available), and thus had a reaction yield of 60%.

A typical discharge curve for a MFC under 1.2V constant potential, using powdered LAH (particle size distribution as-received from the manufacturer), is depicted in Fig 4.6.

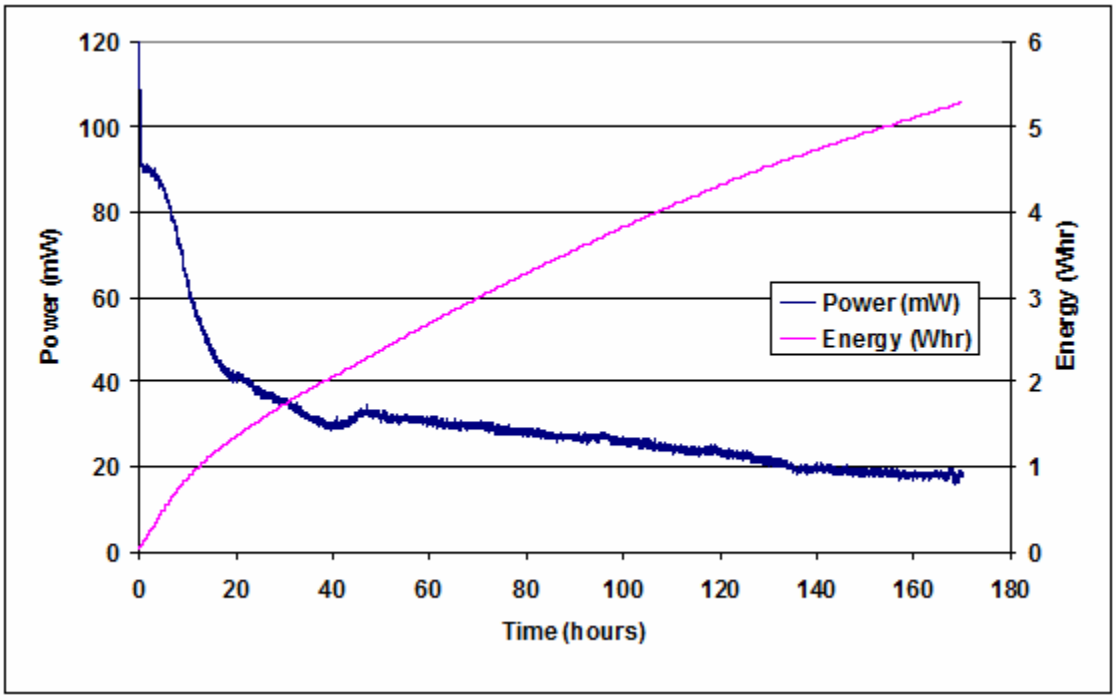

Fig 4.6: 1.2V constant potential discharge of a first generation AA MFC fueled with 2.44g of powdered LAH

Tests in the MFC with powdered LAH exhibit three common characteristics: 1) a short (few minute) initial period of higher power (100-120mW), likely caused by consumption of the initial charge of hydrogen in the fuel chamber 2) a longer period (4-5h) of slightly lower power (80-100mW), as the surface of the powder near the fuel cell is consumed 3) the remainder of the discharge (150-200h) is marked by declining power (an exponential decay) as the void space between the particles is filled with expanding reaction products.

The data in Fig 4.6 was taken for a AA MFC under 1.2V constant potential discharge, and filled with 2.44g of LAH. The MFC delivered 5.30Whr of electrical energy (of 8.28Whr theoretically available), and thus had a reaction yield of 64%. As with crushed

tablets, MFCs discharge with powdered LAH also had relatively low yield due to a significant amount of unreacted LAH remaining in the larger fuel particles at the end of the discharge.

The performance of the MFC with powdered fuel was also evaluated under a 20mA constant current discharge. Fig 4.7 shows a typical discharge curve for a MFC under 20mA constant current using 1.75g of powdered LAH fuel.

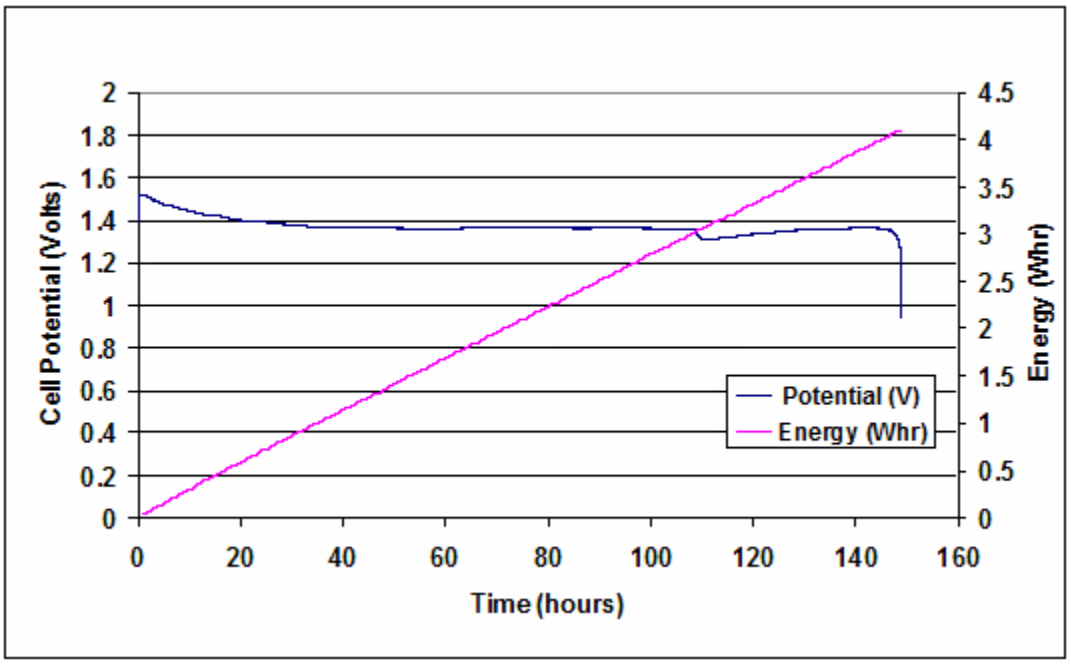

Fig. 4.7: 20mA constant current discharge of first generation AA MFC fueled with 1.75g of powdered LAH

The cell potential was initially 1.5 V, and slowly decayed to 1.35 V after 35 h, where it remained until about 110 h, when it suddenly dropped to about 1.3 V, before recovering slowly to 1.35 V. At 150 h the potential dropped quickly from 1.35 V to the 1 V cutoff,

marking the end of the test, and indicating that the MFC can no longer sustain the 20 mA required by the load.

The potential decay from 1.5 V to 1.35 V during the first 35 h of the test is likely due to atmospheric nitrogen permeating the PEM and reducing the partial pressure of hydrogen in the MFC. A calculation of the nitrogen permeation rate through the PEM under the operating conditions of the MFC indicates that nitrogen partial pressure equilibration with ambient should require ~40 h, indicating that this is a plausible explanation.

The cause of the potential reduction from 1.35V to 1.3V which occurred at ~110h is unknown, however it is hypothesized that the valve may have stuck, causing a temporary reduction in system pressure and cell potential before recovering when the valve became free. It should be possible to confirm this hypothesis in future tests by monitoring the internal pressure and real-time position of the valve throughout the test.

The total energy extracted from the 7.7 cc MFC was 4.1Wh, which corresponds to a system energy density of $532 Whrl^{-1}$. The projected energy in the 1.75 g of LAH fuel is 6.7 Wh, thus the 4.1 Wh of delivered energy corresponds to a LAH reaction yield of 61%. As in the constant potential tests, MFCs tested under constant current discharge also had relatively low yield due to a significant amount of unreacted LAH remaining in the larger fuel particles at the end of the discharge [4.1].

4.5 Second Generation Micro Fuel Cell Performance

Second generation AA MFCs utilize an improved fuel pellet configuration (described in Chapter 3), and demonstrate higher average power, reaction yield, and total extracted energy vs. the first generation devices. The highest performing example (described below) had an energy density of $>1000 Whrl^{-1}$, the highest ever reported in a MFC, and ~3X that of AA alkaline batteries [4.2].

Fig 4.8 shows a typical discharge curve for a second generation MFC under 1.2V constant potential discharge using 2.26g of 5µm LAH fuel.

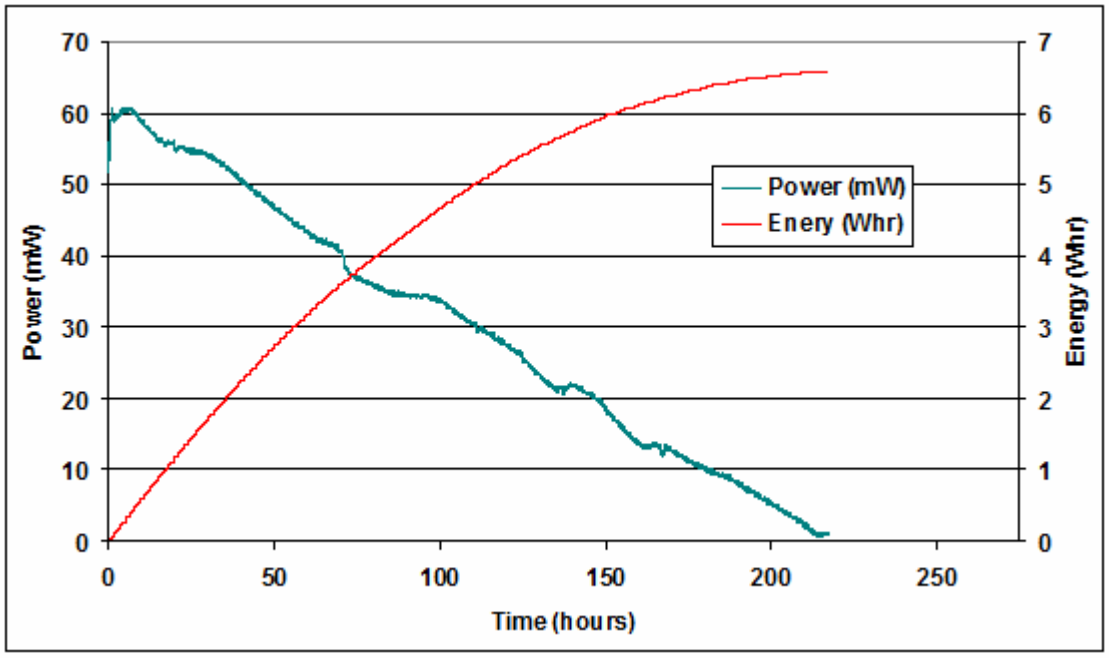

Fig 4.8: 1.2V constant potential discharge of a second generation AA MFC fueled with 2.26g of 5µm LAH

Power output decreased linearly over the discharge, starting at 60mW and decreasing to zero at ~225h. The MFC delivered 6.56Wh of electrical energy (of 7.67Wh

theoretically available), and thus had a reaction yield of 86%. An analysis of the reaction products revealed that the fuel was completely reacted, thus the yield (less than 100%) is attributed to hydrogen leaks in the MFC.

Second generation MFCs with higher fuel density were also tested. Fig 4.9 shows a typical discharge curve for a second generation MFC under 1.2V constant potential discharge using 2.45g of 5µm LAH fuel.

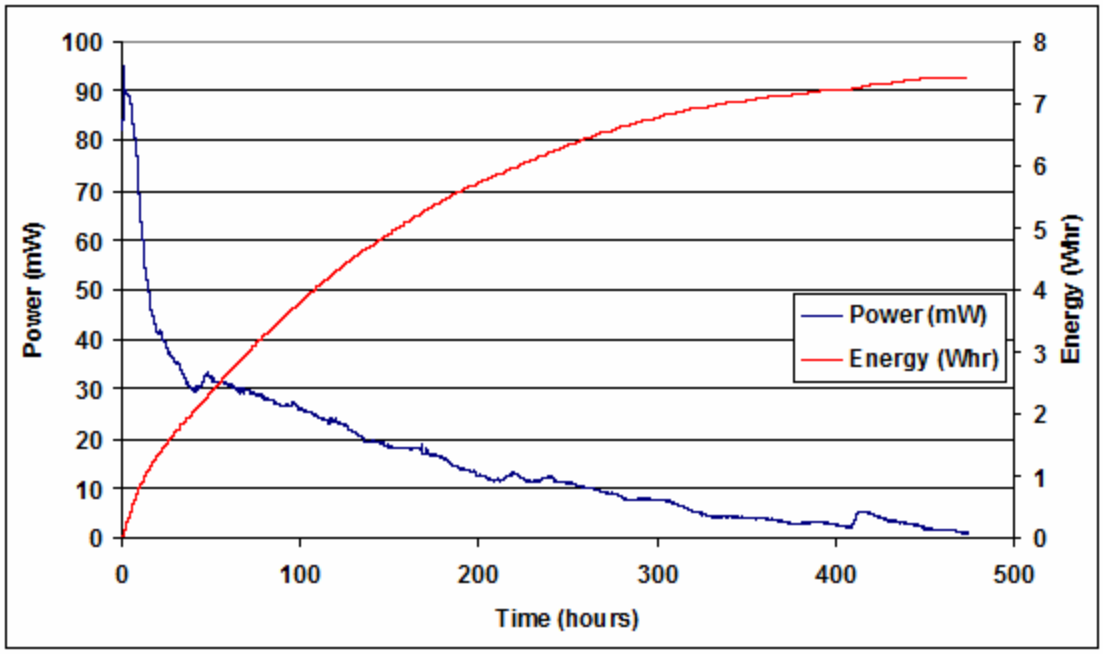

Fig 4.9: 1.2V constant potential discharge of a second generation AA MFC fueled with 2.45g of 5µm LAH fuel

The MFC delivered 7.72Wh of electrical energy (of 8.28Whr theoretically available), and thus had a reaction yield of 93%. This corresponds to system a system energy density

of $1003 Whl^{-1}$. An analysis of the reaction products revealed that the fuel was completely reacted, thus the yield (less than 100%) is attributed to hydrogen leaks in the MFC.

A comparison of yield profiles (yield vs. time) in the MFC (Fig 4.10) for LAH fuel at different particle sizes (5 µm, 20 µm, 50 µm) at a 32% initial void fraction, confirms the results found in the hydrolysis reactor (Chapter 3), namely that smaller particle size (in the range tested) enhances both reaction rate (power) and yield.

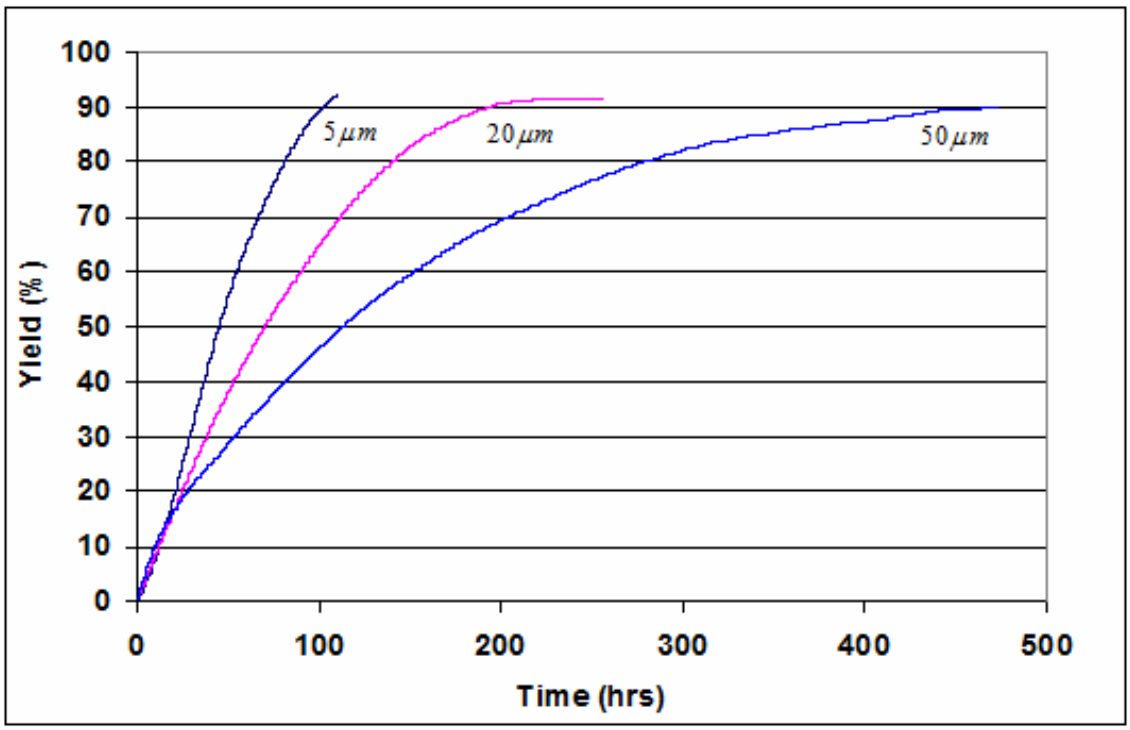

Fig 4.10: Yield profiles at 1.2 V constant potential discharge for the MFC with LAH fuel at three particle sizes (5 µm, 20 µm, 50 µm) at a 32% initial void fraction

Reaction yields for all three particle sizes were greater than 90%, with the 5 µm test yielding 93%, the 20 µm test yielding 91%, and the 50 µm test yielding 90%. These

yields correspond to energy densities of $1003 Whl^{-1}$, $981 Whl^{-1}$, and $971 Whl^{-1}$, respectively, for the 7.7 cc MFC with 2.45 g of LAH fuel (32% initial void fraction in the fuel chamber).

The lower yields of the tests in the MFC, as compared to the hydrolysis reactor, are likely attributed to the small hydrogen leak rates in the MFC, compared to the hermetically sealed hydrolysis reactor (Chapter 3), which had no measurable leak rate. Progressively lower yields for the longer (larger particle sizes) tests support this hypothesis, as does the measured hydrogen leak rate of the empty MFC.

As with the tests conducted in the hydrolysis reactor, the tests in the MFC show the strong impact of particle size on reaction rates, while reaction rates decrease with increasing particle size. Average reaction rates in the MFC were substantially lower (~5X) than in the hydrolysis reactor, as expected, due primarily to the added mass transfer resistance of the PEM in the fuel cell. The dominance of the mass transfer resistance of the PEM is clearly evident during the first 15h of each test, during which the reaction rates were relatively independent of particle size, as indicated by the similar slopes of the yield curves. The curves diverge as the mass transfer resistance of the larger hydride particles begins to dominate the total resistance later in the tests.

Chapter 5: Future Work

The primary goals and objectives of this research have been met: A fully integrated MFC has been developed and demonstrated which meets the physical and electrical requirements of AA batteries while providing significantly (~3X) longer lifetime. These results represent a major step towards realizing the ultimate goal of this research of replacing primary and secondary batteries in portable electronic devices. However, further work must be done to fully realize this goal.

Peak power output of ~150mW was demonstrated in this research, however certain applications including digital cameras, flashlights, and cellular telephones require higher power, and often for extended periods of time. Achieving higher power output in passively regulated MFCs is very challenging due to the diffusion limitation on power output; however several potential avenues exist to increase output, including:

- Patterning the electrocatalyst on the MEA, to separate power generation and water recovery and eliminate the negative effects of osmotic drag on water back-permeation
- Utilize state-of-the-art ionomer membranes which are thinner, move conductive, less permeable to hydrogen, and more permeable to water vapor
- Utilize a “hybrid” fuel formulation of mixed metal hydrides and chemical hydrides, to improve peak power capability

Energy density $1000 Whl^{-1}$ has been demonstrated in this research, however higher energy density should be possible with an improved fuel formulation. Several potential avenues exist to address this including:

- Further exploration of the effects of fuel pellet formulation, (particle size, porosity) geometry, and feature (e.g. spacers) on water vapor transport within the fuel pellet
- Explore the thermodynamics and kinetics of relevant side reactions (e.g. hydrated hydroxide formation, carbonate formation) and identify methods to mitigate their negative effects on power output and energy density
- Build a system level model incorporating all relevant physics, and optimize the fuel pellet configuration for the requirements of portable devices

MFC characterization in this research was limited in scope to a few types of electrical tests (constant potential, constant current) performed under normal ambient conditions (i.e. ~20ºC, 50% RH). Additional characterization is required to understand and optimize the performance of the AA over a broad range of environmental conditions, and to establish safety for use in consumer devices, including:

- Performance evaluation over the full environmental range required by portable devices (temperature, humidity, pressure)
- Evaluate safety to meet requirements for portable devices (shock, vibration, puncture, temperature, immersion in water, etc)

- Gain regulatory for use in portable devices, personal transport, (e.g. on airplanes) etc

The manufacturing cost of the prototype AA MFCs developed in this research is too high to be viable for use in portable devices. Efforts to reduce cost and make the technology viable for high-volume manufacturing will be required, including:

- Redesigning the mechanical components (valve, anode support, cathode electrode) components to enable manufacture via lower-cost methods (e.g. stamping, molding)
- Use of state-of-the-art MEA designs and materials (ionomer, reduced Pt loading, electrocatalyst patterning)
- Developing improved manufacturing processes for the chemical hydride fuels, and scaling to the quantities and formulations (e.g. purity, particle size) required to support their use in high-volume portable devices
- Evaluate the possibility of using replaceable cartridges, to enable reuse of the most expensive components of the MFC (e.g. fuel cell, valve, packaging) while replacing only the consumed portion of the system (e.g. fuel)

References

[1.1] J. A. Paradiso, T. Starner, IEEE Pervasive Computing, 4 (2005) 18-27.

[1.2] International Electrotechnical Commission, [IEC 62282-6-100 Fuel cell technologies, Part 6-100: Micro fuel cell power systems, Safety, Edition 1.0], IEC, Geneva, (2010).

[1.3] S. B. Schaevitz, Proceedings of SPIE, 8248 (2012) 824802-824802.

[1.4]http://www.duracell.com/media/enUS/pdf/gtcl/Product_Data_Sheet/NA_DATASHEETS/MX1500_US_UL.pdf

[1.5] http://www.toshiba.com/taec/news/press_releases/2009/dmfc_09_580.jsp

[2.1] F. Barbir, PEM Fuel Cells: Theory and Practice, Elsevier, Burlington, MA, 2005.

[2.2] E. Chen, Thermodynamics and Electrochemical Kinetics, Fuel Cell Technology Handbook, CRC Press, Boca Raton, FL, 2003

[2.3] J. S. Newman, Electrochemical Systems, Second ed. Prentice Hall, Englewood Cliffs, NJ, 1991.

[2.4] H. A. Gastiger, W. Gu, R Makharia, and M. F. Matthias, Catalyst Utilization and Mass Transfer Limitations in the Polymer Electrolyte Fuel Cells, Tutorial (Electrochemical Society Meeting, Orlando FL, 2003).

[2.5] T. A Zawodzinski et al., Water Uptake by and Transport Through Ionomeric Fuel Cell Membranes, Journal of the Electrochemical Society, 140 (1993) 1981.

[2.6] T. E. Springer et al., Polymer Electrolyte Fuel Cell Model, Journal of the Electrochemical Society, 138 (1991) 2334-2342.

[2.7] T. Fuller and J. Newman, Experimental Determination of the Transport Number of Water in Nafion 117 membrane, Hournal of the Electrochemical Society, 139 (1992) 1332.

[2.8] S. A. Motupally, J. Becher, J. W. Weidner, Diffusion of Water in Nafion 115 Membranes, Journal of the Electrochemical Society, 147 (2000) 3171.

[3.1] Schlesinger, H. I.; Brown, H. C.; Finholt, A. E.; Gilbreath, J. R.; Hoekstra, H. R.; Hyde, E. K., "Sodium Borohydride, Its Hydrolysis and its Use as a Reducing Agent and in the Generation of Hydrogen." J. Am. Chem. Soc. 75 (1953) 215–219.

[3.2] W. D. Davis, S. L. Mason, G. Stegeman, "The Heats of Formation of Sodium Borohydride, Lithium Borohydride, and Lithium Aluminum Hydride." *J. Am. Chem. Soc.* 71*(*1949) 2775–2781.

[3.3] V.C.Y. Kong, F.R. Foulkes, Development of hydrogen storage for fuel cell generators. I: hydrogen generation using hydrolysis hydrides, Int. J. Hydrogen Energy 24 (1999) 665–675.

[3.4] V. C. Kong, D. W. Kirk, F.R. Foulkes, J. T. Hinatsu, Development of hydrogen storage for fuel cell generators II: utilization of calcium hydride and lithium hydride Int. J. Hydrogen Energy 28 (2003) 205-214

[3.5] C. Maupoix, J. L. Houzelot, E. Sciora, Experimental investigation of the grain size dependence of the hydrolysis of LiH powder, J. Powder Tech. 208 (2011) 318–323

[3.6] A. Veerman, H. M. Lee, K. S. Kim, Dissolution nature of lithium hydroxide by water. J. Chem. Phys. 123 (2005) 084321.

[3.7] A. Broughton: ‘Hydrolysis of lithium hydride’, PhD thesis, University of Reading, UK, 2001.

[3.8] I. H. MacPherson, Hydride as a Storage Medium. HIC Report, 1992

[3.9] L. H. Thomas, D. J. Holve, In-process particle size distribution measurements and control. Part. Part. Syst. Charact. 10 (1993) 262–265.

[3.10] Y. Kojima, K. I. Suzuki, Y. Kawai, “Hydrogen generation by hydrolysis reaction of magnesium hydride,” Journal of Materials Science 39 (2004) 2227–2229

[4.1] S. Eickhoff, C. Zhang, T. Cui, Micro fuel cell utilizing fuel cell water recovery and pneumatic valve, Journal of Power Sources, 240 (2013) 1-7.

[4.2] S. Eickhoff, C. Zhang, T. Cui, The effects of hydride chemistry, particle, size, and void fraction of micro fuel cell performance, Journal of Power Sources, 243 (2013) 562-568.